Journal of the Mechanics and Physics of Solids 144 (2020) 104103

Contents lists available at ScienceDirect

Journal of the Mechanics and Physics of Solids

journal homepage: www.elsevier.com/locate/jmps

Investigating the incremental behavior of granular materials with the level-set discrete element method

Konstantinos Karapiperis[a], John Harmon[a], Edward Andò[b], Gioacchino Viggiani[b], José E. Andrade[a,*]

[a] Division of Engineering and Applied Science, California Institute of Technology, Pasadena, CA 91125, USA
[b] Univ. Grenoble Alpes, CNRS, Grenoble INP, 3SR, F-38000 Grenoble, France

ARTICLE INFO

Article history:
Received 26 April 2020
Revised 6 July 2020
Accepted 30 July 2020
Available online 8 August 2020

Keywords:
Granular mechanics
Virtual experiments
Discrete element method
Plasticity

ABSTRACT

A computational framework is presented for high-fidelity virtual (in silico) experiments on granular materials. By building on i) accurate mathematical representation of particle morphology and contact interaction, ii) full control of the initial state of the assembly, and iii) discrete element simulation of arbitrary stress paths, the proposed framework overcomes important limitations associated with conventional experiments and simulations. The framework is utilized to investigate the incremental response of sand through stress probing experiments, focusing on key aspects such as elasticity and reversibility, yielding and plastic flow, as well as hardening and fabric evolution. It is shown that reversible strain envelopes are contained within elastic envelopes during axisymmetric loading, the yield locus follows approximately the Lade-Duncan criterion, and the plastic flow rule exhibits complex nonassociativity and minor irregularity. Hardening processes are delineated by examining the stored plastic work and the fabric evolution in the strong and weak networks. Special attention is given to isolating in turn the effect of particle shape and interparticle friction on the macroscopic response. Interestingly, idealization of particle shape preserves qualitatively most aspects of material behavior, but proves quantitatively inadequate especially in anisotropic stress states. The results point to the importance of accurately resolving particle-scale interactions, that allows macroscopic behavior to emerge free from spurious micromechanical artifacts present in an idealized setting.

1. Introduction

The continuum response of a granular assembly is encoded in the evolving kinematics of particles, driven by frictional forces at discrete interparticle contacts. Decoding this response experimentally is fraught with difficulties mainly in extracting interparticle forces, and creating reproducible conditions. The Discrete Element Method (DEM) (Cundall and Strack, 1979) has provided a numerical framework that overcomes these difficulties, but at the same time introduces new limitations, due to the idealization of granular shape or the incorporation of questionable rolling dissipation (Ai et al., 2011). Recently, a pivotal advancement that overcomes these limitations has been achieved though the level-set characterization of the morphology of individual grains using X-ray Computed Tomography (XRCT) (Vlahinić et al., 2014), and its utilization within the

* Corresponding author.
E-mail address: jandrade@caltech.edu (J.E. Andrade).

https://doi.org/10.1016/j.jmps.2020.104103
0022-5096/

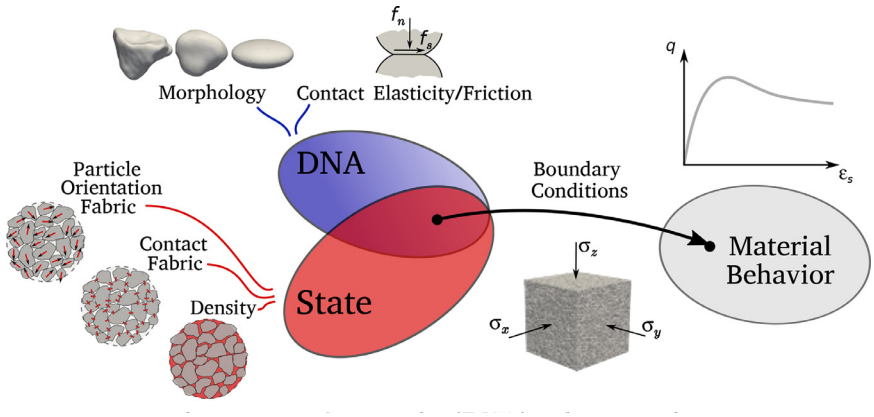

Fig. 1. The concept of a granular 'DNA' within virtual experiments.

Level-Set DEM (LS-DEM) framework (Kawamoto et al., 2016). Even more recently, significant steps have been made in validating the method (Karapiperis et al., 2020; Kawamoto et al., 2018; Li et al., 2019), thus paving the way for a systematic investigation of granular behavior through high-fidelity virtual experiments.

The cornerstone of experiments on granular matter is stress probing, which relies on achieving multiple incremental stress paths originating from an identical initial state. Physical stress probing experiments are extremely hard to conduct, which explains the scarcity of relevant studies (Anandarajah et al., 1995; Royis and Doanh, 1998). On the other hand, numerical stress probing via conventional DEM (e.g. Bardet, 1994; Calvetti et al., 2003a; Tamagnini et al., 2005; Wan and Pinheiro, 2013) has served as an effective platform for the investigation of constitutive behavior in a qualitative sense. The first DEM stress probing experiments were conducted by Bardet (1994) using disks. Later, Calvetti and coworkers carried out similar experiments with spheres, and used them to examine the importance of preloading (Calvetti et al., 2003a), inspect the underlying micromechanics (Calvetti et al., 2003b), and assess different classes of continuum theories (Tamagnini et al., 2005). In several occasions (e.g. when probing from a preloaded state), they identified deviations from classical plasticity in the form of a nonregular flow rule, which was interpreted as evidence of thorough incremental nonlinearity (e.g. hypoplasticity) (Tamagnini and Viggiani, 2002). This was in line with later observations in (Kuhn and Daouadji, 2018; Wan and Pinheiro, 2013). The influence of triaxiality on the regularity of the flow rule was investigated in (Wan and Pinheiro, 2013), while the effect of the rotation of principal stresses was discussed in (Froiio and Roux, 2010). A critical element in analyzing results of numerical (or virtual) stress probing experiments is the decomposition between elastic and plastic strains. These have been typically extracted either by unloading to the initial state (Bardet, 1994), or by carrying out additional simulations where dissipative mechanisms are inhibited (Calvetti et al., 2003a; 2003b; Tamagnini et al., 2005). Wan and Pinheiro (2013) have suggested that the two approaches are equivalent. On the other hand, Kuhn and Daouadji (2018) observed that the two approaches produce different decompositions, and examined the relevant implications within the context of a thermodynamical framework, complementing an earlier discussion in (Collins and Einav, 2005). With the exception of a 2D polygon study in (Alonso-Marroquín et al., 2005), all the aforementioned studies involve highly idealized particle shapes (disks or spheres).

The first objective of this paper is to introduce a new paradigm of virtual experiments building on the recent development of LS-DEM (Section 2). The framework incorporates an unprecedentedly accurate representation of particle morphology and interaction, which jointly define a type of granular 'DNA'. By controlling the expression of that 'DNA' to a desired configurational state - a process intractable with preexisting techniques - and evolving that state by imposing arbitrary stress paths, the proposed framework is established (Fig. 1). In Section 3, the framework is utilized to systematically investigate the incremental response of an angular sand through multiple stress probing experiments. In a first set of axisymmetric experiments, the elastic-plastic and reversible-irreversible decompositions of strain are investigated, and the properties of plastic flow are discussed as functions of the current state and its history. We, then, shed light on the micromechanical processes driving dissipation, hardening and fabric evolution, and briefly examine the relevant role of fluctuations. Subsequent experiments focus on isolating the effect of interparticle friction and particle morphology, and assessing the effect of the common spherical idealization. In a final set of deviatoric experiments, we map the entire yield surface in 3D principal space and quantify the nonassociativity of the flow rule as a function of the mean stress and Lode angle. A discussion of the main findings and the future potential of virtual experiments, in Section 4, concludes this paper.

2. Virtual experiments

Physical experiments of granular materials suffer from poor reproducibility and limited control of initial and boundary conditions. They also inherently lack the ability to measure interparticle forces, a key ingredient in understanding the constitutive behavior. The proposed in silico experiment framework effectively bypasses these limitations by relying on a) the

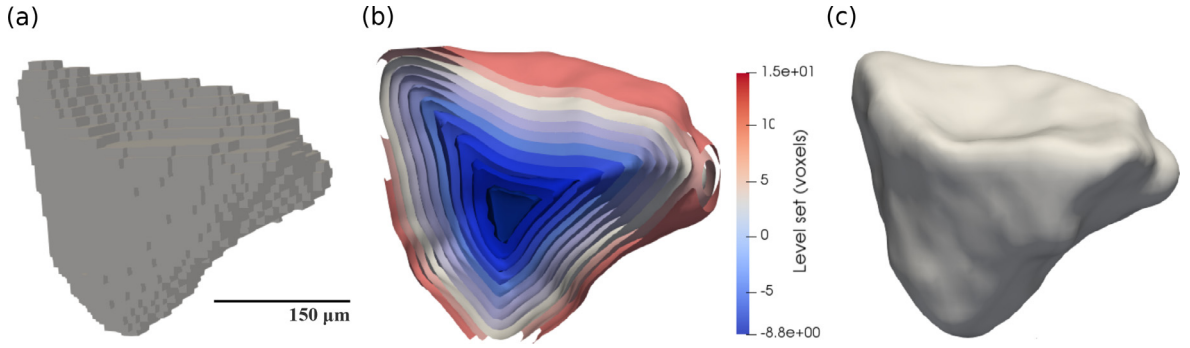

Fig. 2. a) Hostun sand grain segmented from XRCT, b) Slice of grain level set (blue: interior, red: exterior), and c) Particle surface. (For interpretation of the references to colour in this figure legend, the reader is referred to the web version of this article.)

accurate mathematical description of particle morphology and interaction, b) the control of the initial state of the assembly and c) the enforcement of boundary conditions following an experimental protocol.

2.1. Particle morphology and interaction

The mathematical representation of particle geometry is achieved through mathematical objects termed level sets (Kawamoto et al., 2016). Given a local (particle) coordinate system, the value of a level set function $\phi(\mathbf{x})$ is the signed distance from a point $\mathbf{x}$ to the grain's surface, described by the zero-level set $\{\mathbf{x} \,|\, \phi(\mathbf{x}) = 0\}$. Such functions may either be constructed using standard level set operations (Osher and Fedkiw, 2003) or extracted directly from XRCT images using level set imaging techniques (Vlahinić et al., 2014), given the increased resolution of modern 3D XRCT technology (Andò et al., 2013; Cil et al., 2017). An example of extracting a level set of an angular sand grain is given in Fig. 2. From a collection of grain morphologies, a distribution of geometrical properties spanning multiple scales (e.g. sphericity, roundness) may be obtained. Finally, this distribution can be sampled to produce granular clones of similar morphology (Buarque de Macedo et al., 2018).

The granular 'DNA' can be described by these morphological distributions, complemented by interparticle contact laws and associated grain-scale material properties. A general description of interparticle contact is furnished by thermodynamics; for a discrete contact point c, one can consider a Gibbs energy $G^c(\mathbf{f}^c, \mathbf{q}^c, \theta)$ as a function of the contact force $\mathbf{f}^c$, the temperature θ and an internal variable $\mathbf{q}^c$ related to dissipative events (sliding displacement/contact damage), and an associated contact dissipation potential ψ^c, in analogy to continuum thermodynamics (Onsager, 1931; Ortiz, 2012; Ziegler, 1977). Presented in Appendix A is a simple formalism, from which various contact laws may be derived. Note that the material properties on which they rely (e.g. interparticle friction, contact stiffness) may now be directly measured at the grain-scale by means of compressive (Cole and Peters, 2007), shearing (Cavarretta et al., 2010; Senetakis et al., 2013) and multidirectional (Nardelli and Coop, 2018) tribological experiments conducted between individual particles.

2.2. Control of initial state

Once the granular 'DNA' is fully characterized, the next step is to control its expression to a configurational state, that includes initial stress, density and contact-/particle orientation-fabric. The state may be either obtained using imaging techniques in an *in-situ* XRCT experiment (Kawamoto et al., 2018), or, more generally, it may generated by simulating a preparation protocol designed to target particular state properties. The latter relies on simulating particle interaction, through a level-set based discrete element framework, termed LS-DEM (Kawamoto et al., 2016). Similarly to the original DEM formulation (Cundall and Strack, 1979), LS-DEM resolves the kinematics of grains whose interaction is governed by contact mechanics, but at the same time is able to represent realistic grain shape. At each time step and contact point, the contact force $\mathbf{f}^c$ is computed based on the interaction law, and contributes to a moment $\mathbf{m}^c$ about the particle's center of mass. Given the inertial properties of the particle, its kinematics are updated using an appropriate time integration scheme of Newton's equations of motion. For a detailed explanation of the LS-DEM framework the interested reader is referred to (Kawamoto et al., 2016).

Fig. 3 shows an example preparation protocol using LS-DEM, where grains are being pluviated from an orifice into a cubical container. By controlling the height and supply rate of pluviation, as well as the orientation of the container, a desired packing fraction and fabric may be achieved. Importantly, the complete description of fabric involves not only on the orientational distribution of contacts - the most common way of quantifying fabric to date (O'Sullivan, 2011) - but also on the distribution of particle orientations or voids, which is intractable with conventional methods (e.g. DEM). We refer to Section 3.1 for an example of fabric quantification within the proposed framework.

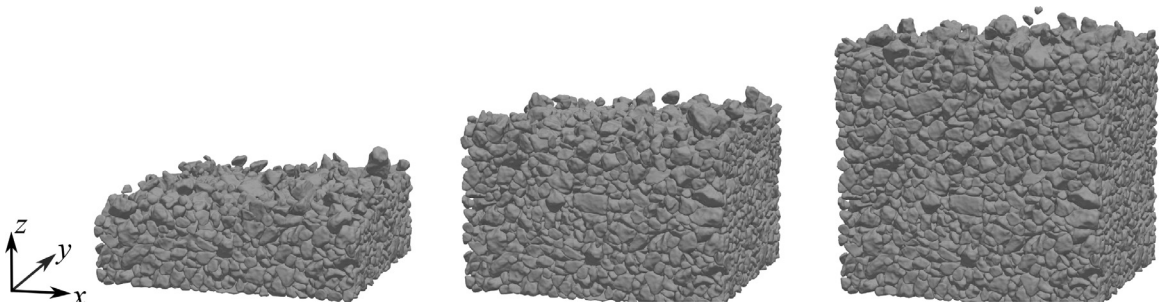

Fig. 3. Stages of virtual pluviation of a sample of Hostun sand.

Table 1
Particle properties used in the virtual experiments.

Parameter	Value	Units
Density (ρ)	2500	Kg/m^3
Normal stiffness (k_n)	$3 \cdot 10^4$	N/m
Shear stiffness (k_t)	$2.7 \cdot 10^4$	N/m
Friction coefficient (μ)	0.4	-
Coefficient of restitution (c)	0.6	-

2.3. Testing protocol

The power of virtual experiments is fully exploited in the testing phase, since they enable the exact replication of any generated initial state and the enforcement of arbitrary mixed boundary conditions. For example, true triaxial conditions (Section 3.9) can be easily established without the need for complicated experimental design (Reddy et al., 1992). Before enforcing such conditions and embarking on a systematic exploration of stress space, it is necessary to establish confidence in the method within conventional stress paths. Indeed, LS-DEM has recently been validated against physical triaxial compression (Kawamoto et al., 2018) and shear experiments (Li et al., 2019), where parameters were directly computed from particle material properties and the initial state was replicated using level-set imaging. The method was able to capture quantitatively the macroscopic (stress-strain), mesoscopic (spatiotemporal prediction of onset and evolution of a shear band and its kinematics), and particle-scale response (contact-normal and force distribution, and friction mobilization).

3. Stress probing

3.1. Setup

This section details the virtual experiment setup used to investigate the incremental response of an angular sand. The model consists of 15625 virtual Hostun sand grains[1], whose morphology has been extracted from μ-XRCT data (Section 2.1). The grain interaction follows a Hookean elastic - Coulomb frictional law (Appendix A), with the relevant properties given in Table 1. To accelerate the approach to equilibrium, contact damping with a coefficient of restitution of 0.6 is introduced in the interaction law. Additional experiments verified that the results were insensitive to the choice of coefficient of restitution, under a sufficiently low dimensionless inertial number ($I \leq 10^{-3}$).

We employ LS-DEM to simulate both specimen preparation and stress probing. Via dry pluviation we construct a dense cubical assembly of virtual Hostun sand particles (Fig. 4) of relative density $D_r = 85\%$ and corresponding void ratio $e = 0.55$. To calculate the relative density, the minimum and maximum void ratios were first estimated based on the following protocols. The densest state was reached by pluviating particles into a container under gravity, and subsequently subjecting the container to vertical sinusoidal vibration at 60 Hz under constant vertical load, until the void ratio plateaued to a value $e_{\min} = 0.51$. This method is similar to that described in the ASTM standards (ASTM International, 2006; Chang et al., 2017). Accordingly, the loosest state was obtained by pluviation from zero height (ASTM International, 2016; Vaid and Negussey, 1984), followed by compression to the same vertical load for consistency with the dense measurement, resulting in a void ratio $e_{\max} = 0.74$.

Remark 1. The experimentally reported values for Hostun sand are $e_{\min} = 0.656, e_{\max} = 1.0$ (Doanh and Ibraim, 2000), yielding an equivalent void ratio $e = 0.71$. Note that these values are higher than our simulated values reported above. This is due to using a different GSD by utilizing few distinct morphologies repeated in the sample to reduce memory requirements.

[1] Increasing sample sizes were used to ensure that the size of the unit cell is representative (see Appendix B).

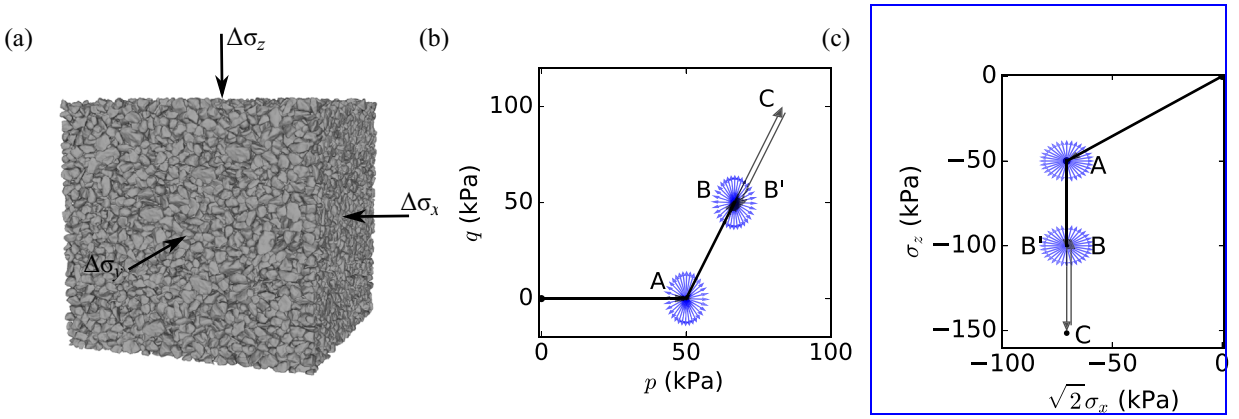

Fig. 4. a) Virtual specimen of Hostun sand under three dimensional stress conditions. b) Imposed stress states and probing protocol in p-q plane c) Same in the Rendulic plane.

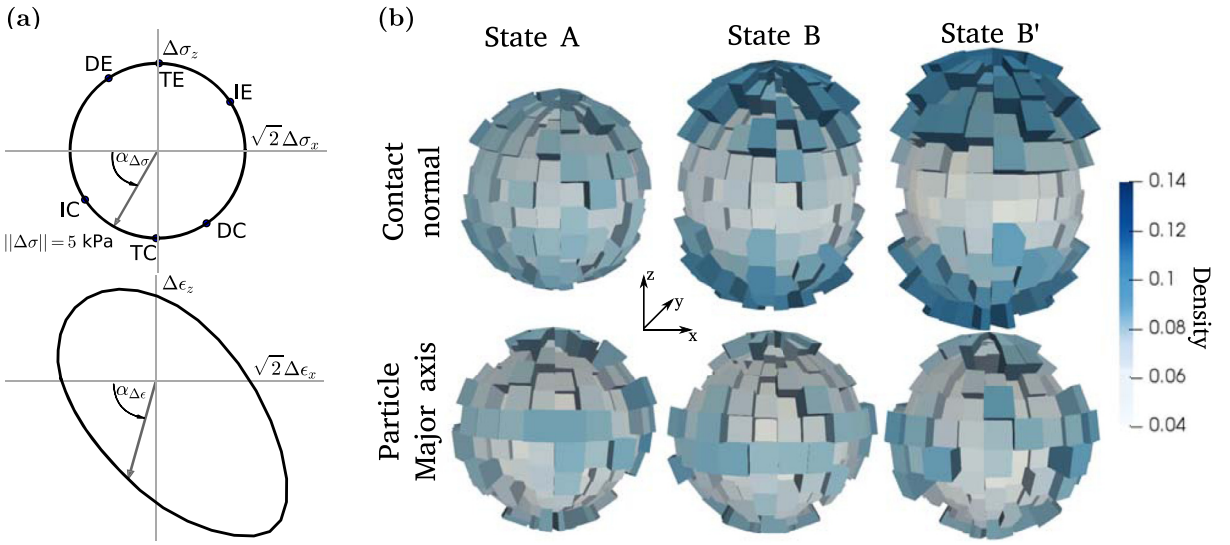

Fig. 5. a) Top: Stress probing paths form a circle in the Rendulic plane of stress increments. Marked characteristic paths: isotropic (IE), triaxial (TE) and deviatoric (DE) extension, isotropic (IC), triaxial (TC) and deviatoric (DC) compression. Bottom: Sketch of the strain response in the Rendulic plane of strain increments. b) Contact-normal and major particle axis orientation fabric at states *A*, *B* and *B*′.

After pluviation, each specimen is isotropically consolidated to state *A* by applying a uniform confining pressure of $p_A = 50$ kPa. Note that the sign convention of solid mechanics (compression negative) is adopted here, and we define $p = -1/3\,\mathrm{tr}\boldsymbol{\sigma}$, $q = \sqrt{3/2\,\boldsymbol{s}:\boldsymbol{s}}$ where $\boldsymbol{s} = \boldsymbol{\sigma} + p\boldsymbol{I}$. The confining pressure is applied using numerical servocontrol to adjust the displacement of the surrounding walls, which are modelled as smooth frictionless elements.[2] This ensures that the principal axes of stress and strain are coincident with the axes of the cube (Fig. 4a)) (Calvetti et al., 2003a). Afterwards a drained triaxial compression along the *z*-direction is imposed at constant lateral stress $\sigma_X = \sigma_Y$ until an anisotropic state *B* ($q_B = 50$ kPa), termed the *virgin* state, is reached. Finally, the samples are subjected to further drained triaxial compression to state *C* ($q_C = 100$ kPa), and unloaded to produce the *preloaded* state *B*′ ($q_{B'} = 50$ kPa). The packing and history at states *A*, *B* and *B*′ are stored and cloned (Alonso-Marroquín et al., 2005), since each will serve as the initial condition of a subsequent axisymmetric stress probing protocol (Fig. 4 b,c)). The latter consists of 32 axisymmetric probes, uniformly distributed in the Rendulic angle $\alpha_{\Delta\boldsymbol{\sigma}} = \arctan(\Delta\sigma_z/\ \sqrt{2}\Delta\sigma_x) \in [0^\circ, 360^\circ)$, each with a Euclidean norm of 5 kPa, forming a circle in the Rendulic plane (Fig. 5a)). Characteristic probes include: isotropic (IE), triaxial (TE) and deviatoric (DE) extension, as well as isotropic (IC), triaxial (TC) and deviatoric (DC) compression. Similarly to earlier studies, the stress states and probing

[2] An alternative way to impose the stress state is through periodic boundary conditions. This is avoided in this study since it imposes constraints on the sample preparation procedure, which in this particular case is non-periodic.

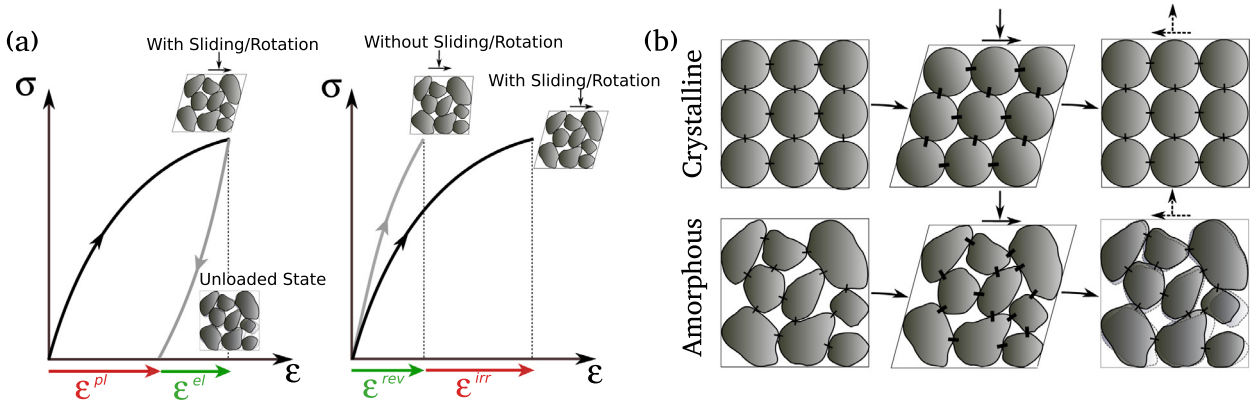

Fig. 6. a) Elastic-plastic (left) and reversible-irreversible strain decomposition (right) b) Incremental response of a crystalline vs an amorphous assembly upon a loading-unloading cycle.

magnitudes/angles were chosen such that the effect of anisotropy and history is adequately captured while minimizing computational demands.

Before analyzing the stress probing response, we quantify the state of the sample beyond the isotropic measure of relative density discussed above. To this end, Fig. 5 b) shows the orientation histograms for the contact-normals and major particle orientation axes, computed at all states. The sample exhibits initially (state A) only a slight vertical fabric anisotropy, which becomes increasingly pronounced at the anisotropic states B, B'. On the other hand, the particle orientation fabric remains approximately isotropic throughout the experiment.

3.2. Scope

In the remaining sections, we will focus on gaining insight into i) the strain response due to stress probing, mathematically summarized as $d\boldsymbol{\epsilon} = \mathcal{S}(\boldsymbol{\sigma}, \boldsymbol{\eta}, \mathbf{q}) : d\boldsymbol{\sigma}$, where $\boldsymbol{\eta}$ is the stress probing direction, and $\mathbf{q}$ is some representation of the internal state, and ii) the evolution of the internal state due to probing, succinctly given as $d\mathbf{q} = \mathcal{H}(\boldsymbol{\sigma}, \boldsymbol{\eta}, \mathbf{q}) : d\boldsymbol{\sigma}$.

3.3. Strain response

Fig. 6 a) shows two decompositions of the strain response considered in this study. In order to define the *elastic-plastic* strain decomposition, we follow the work of Bardet (1994), where the plastic strain is identified as the residual strain upon unloading to a reference stress state. The elastic strain is, then, recovered by subtracting the residual from the total strain. On the other hand, the *reversible-irreversible* decomposition partitions the strain into that arising from reversible and irreversible grain-scale mechanisms. The reversible response is furnished by an additional set of stress probing experiments in which frictional dissipation (slip) has been inhibited (Calvetti et al., 2003a). The irreversible component follows by subtracting the reversible from the total strain response.

As illustrated schematically in Fig. 6b), the *elastic-plastic* and the *reversible-irreversible* decompositions may only coincide in a perfectly *crystalline* arrangement. Indeed, in that case, the applied loading induces an affine deformation of the contacts, which is exactly reversed upon unloading. On the contrary, during loading of an *amorphous* assembly, fluctuations are known to develop (Richefeu et al., 2012), leading to some contacts behaving elastically, and others sliding variably. Upon unloading, the contact deformations are not exactly reversed, as measured in a virtual experiment and shown in Appendix C. This results in an altered configuration, and, hence, the divergence between elastic and reversible response. Macroscopically, this divergence manifests itself as elastic-plastic coupling (Collins and Einav, 2005; Hueckel, 1976; Kuhn and Daouadji, 2018).

3.3.1. Elastic-plastic strain decomposition

Figs. 7, 8 and 9, show the total, elastic and plastic strain response envelopes (Gudehus, 1979) obtained in this manner for stress probes originating at states A, B and B' respectively. The plot insets show the stress-strain response for specific probes, revealing different amounts of hysteresis depending on the probing direction. A few observations can be made:

- To a first approximation, the total strain envelope at state A is given by an ellipse, while the same envelopes at states B and B' are given by two sections of ellipses, one in the direction of deviatoric compression (DC) and another in the direction of deviatoric extension (DE).
- The elastic envelopes form ellipses, which, for anisotropic states (B, B'), are coincident with the corresponding total strain envelopes in the direction of previous loading history, essentially corresponding to stress reversal (DE, DC respectively).
- The elastic envelopes are approximately centered at the origin of the Rendulic plane. Non-centricity is more pronounced in the case of anisotropic states.

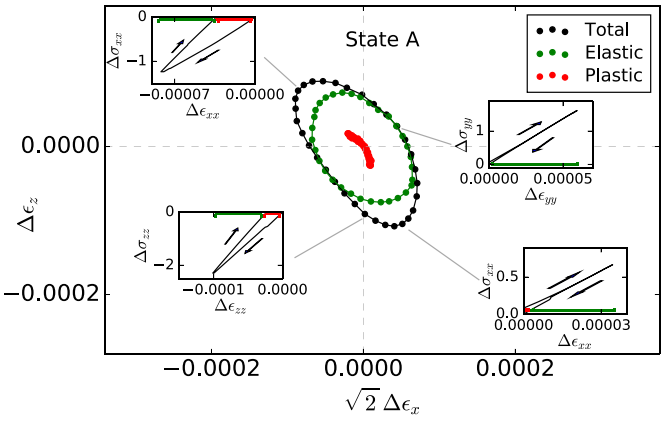

Fig. 7. Total (black), elastic (green), and plastic (red) strain response envelopes for the dense specimen at *isotropic state A*. Insets: Loading/Unloading stress-strain curves. (For interpretation of the references to colour in this figure legend, the reader is referred to the web version of this article.)

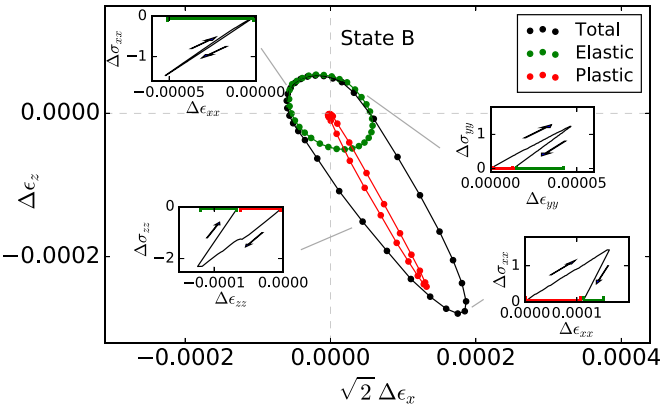

Fig. 8. Total (black), elastic (green), and plastic (red) strain response envelopes for the dense specimen at *virgin state B*. Insets: Loading/Unloading stress-strain curves. (For interpretation of the references to colour in this figure legend, the reader is referred to the web version of this article.)

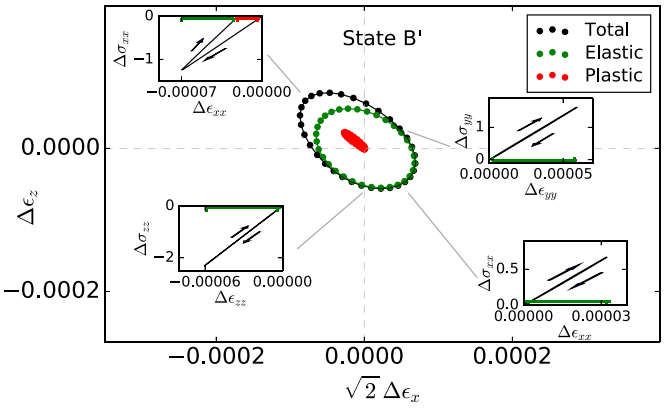

Fig. 9. Total (black), elastic (green), and plastic (red) strain response envelopes for the dense specimen at *preloaded state B′*. Insets: Loading/Unloading stress-strain curves. (For interpretation of the references to colour in this figure legend, the reader is referred to the web version of this article.)

- An approximately unique plastic strain increment direction is observed, which is distinct for each state, suggesting incremental bilinearity (Calvetti et al., 2003a). Yet, closer inspection reveals some degree of deviation in the form of angle dependence for all states. Particularly, at state *A*, this deviation could be attributed to the presence of a minor vertical fabric.
- The principal axes of the total, elastic and plastic envelopes are noncoaxial. This is related to the nonassociativity of the plastic flow rule which is quantified for all three states in Fig. 10. The latter shows the average orientation of the

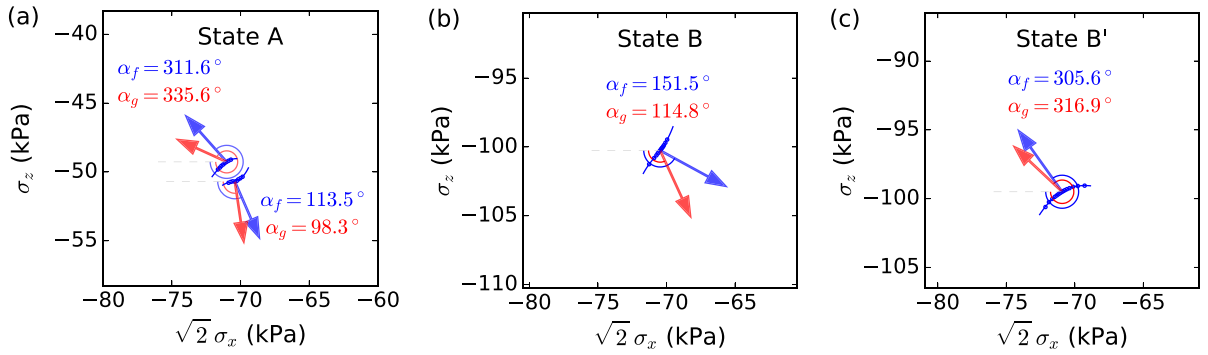

Fig. 10. Average orientation of yield surface normals (blue) and plastic potential normals (red) in the Rendulic stress plane for (a) the isotropic state *A*, (b) the anisotropic state *B* and (c) the preloaded state *B*′. Blue dots represent the trace of the yield surface. (For interpretation of the references to colour in this figure legend, the reader is referred to the web version of this article.)

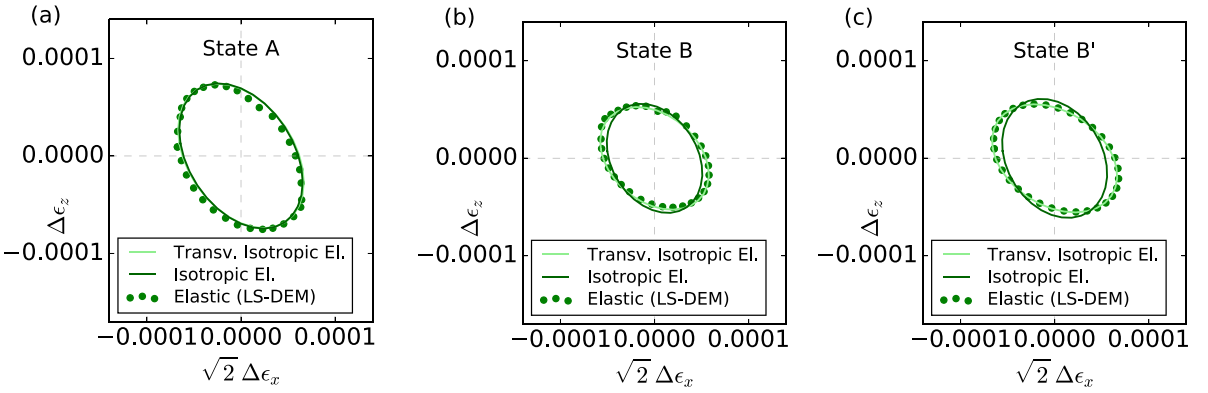

Fig. 11. Elastic envelopes obtained from the virtual experiments compared to the linear elastic isotropic- and transversely isotropic fitted envelopes for (a) the isotropic state *A*, (b) the anisotropic state *B* and (c) the preloaded state *B*′.

Table 2
Measured elastic parameters for isotropic- and transversely isotropic elasticity.

Model	Parameter	A	B	B'
Isotropic Elastic	E (MPa)	**34.1**	45.1	41.2
	ν	**0.149**	0.113	0.106
Transversely Isotropic Elastic	E_x (MPa)	34.2	**13.2**	**14.6**
	E_z (MPa)	34.1	**48.2**	**45.8**
	ν_x	0.151	**0.698**	**0.616**
	ν_{zx}	0.147	**0.146**	**0.154**

normal to the implied yield surface (interpreted as the locus of stress states corresponding to the same norm of plastic strain rate) and the orientation of the normal to the plastic potential (i.e. the average orientation of the plastic strain rate). Their difference is a measure of the nonassociativity of the flow, which appears to be most pronounced in the anisotropic state *B*.

- By comparing the elastic envelopes at the three states (Fig. 11), we observe an increase in elastic stiffness, and the development of elastic anisotropy at states *B* and *B*′, compared to state *A*. The elastic response in each state is quantified by fitting linear elastic isotropic- and transversely isotropic envelopes, as described in Appendix D. The relevant parameters are tabulated in Table 2.

3.3.2. Reversible-irreversible strain decomposition

Fig. 12 shows, for all three states, the reversible, irreversible and total strain response envelopes obtained via inhibited-dissipation experiments. We observe that:

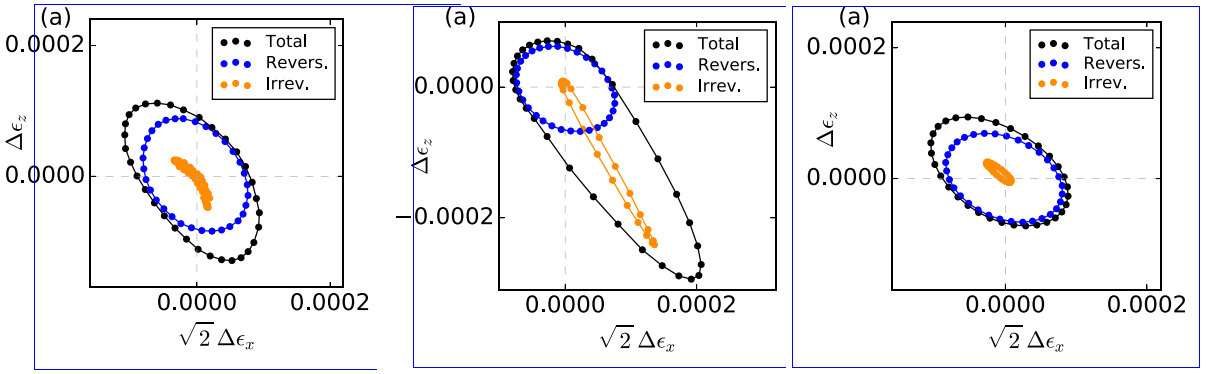

Fig. 12. Total (black), reversible (blue) and irreversible (orange) strain response envelopes in the Rendulic stress plane for (a) the isotropic state A, (b) the anisotropic state B and (c) the preloaded state B'. (For interpretation of the references to colour in this figure legend, the reader is referred to the web version of this article.)

- Reversible strain envelopes form ellipses that are very similar yet slightly smaller than the elastic ones. They are generally contained within the elastic envelopes.
- The difference between elastic and reversible strain, which can be identified as a coupled strain (Kuhn and Daouadji, 2018), is most pronounced along the directions of (DC) and (DE).
- Irreversible strains generally arise for almost all Rendulic angles, with the exception of isotropic compression (IE) and isotropic extension (IE). The direction of the irreversible strain rate is only weakly dependent on the probing angle, which defines a slightly irregular flow rule (Wan and Pinheiro, 2013).
- For any given state, irreversible and plastic strain increment directions generally coincide.
- Preloading leads to a stiffness increase along the (DC) direction, evidenced by the corresponding reduction in total strain. As a result, total and irreversible strain envelopes become more symmetric at B' compared to B.

Remark 2. In extracting the reversible response through such numerical experiments, one needs to ensure that no irreversible changes occur in the contact topology (creation and extinction of contacts). However, this condition cannot be guaranteed *a priori* by only inhibiting interparticle dissipation (slip). Our approach is to accept that some minor topological changes will occur, and then quantify the extent of these topological changes on the response *a posteriori*. To do so, we consider the stress increment during a probe (Christoffersen and Hutchinson, 1979):

$$\Delta\boldsymbol{\sigma} = \boldsymbol{\sigma}' - \boldsymbol{\sigma} = \sum_{c\in\mathcal{C}'} \mathbf{f}'_c \otimes \mathbf{l}'_c - \sum_{c\in\mathcal{C}} \mathbf{f}_c \otimes \mathbf{l}_c \tag{1}$$

where $\mathbf{f}_c$, $\mathbf{l}_c$ denote the force and branch vectors at the initial configuration, and $\mathbf{f}'_c, \mathbf{l}'_c$ denote those at the configuration after probing. The sets $\mathcal{C}, \mathcal{C}'$ represent the collection of contacts at the two configurations. We can rewrite Eq. (1) to obtain the following decomposition:

$$\Delta\boldsymbol{\sigma} = \sum_{c\in\mathcal{C}\cap\mathcal{C}'} (\mathbf{f}'_c \otimes \mathbf{l}'_c - \mathbf{f}_c \otimes \mathbf{l}_c) + \sum_{c\in\mathcal{C}'\setminus\mathcal{C}} \mathbf{f}'_c \otimes \mathbf{l}'_c - \sum_{c\in\mathcal{C}\setminus\mathcal{C}'} \mathbf{f}_c \otimes \mathbf{l}_c \tag{2}$$

where the first term arises from two reversible mechanisms: i) the change in interparticle forces under fixed topology and ii) the change in fabric due to dissipation-free particle rolling. The second and third terms are due to the change in topology via creation and loss of contacts respectively, and represent irreversible mechanisms. We find that these last two terms consistently contribute less than 5% to the stress increment. Hence, we conclude that this approach yields a good (slighty overestimated) approximation of the reversible response.

In Appendix E, two additional strategies for the estimation of the reversible response are presented: i) a similar numerical construction where particle rotations are also constrained, and ii) an analytical homogenization-based approach. These methods are shown to provide lower bounds for the reversible response, and are not pursued further.

3.4. Hardening and stored plastic work

In order to shed light on hardening processes, we discuss here the thermodynamics of deformation during a closed cycle. To do so, we compute the change in the stored elastic energy $U^{el} = \sum_c U^{el,c}$ and the dissipation increment as $d\psi = \sum_c d\psi^c$, where the summation takes place over all contacts. Fig. 13a) shows the frictional dissipation in the sample, normalized with the initial stored elastic energy $U^{el,0}$, against the Rendulic angle during loading and unloading probes from the isotropic state A. We observe that dissipation is present throughout all angles, yet attains its maximum in the (DC) and (DE) directions at both loading and unloading. Fig. 13b) shows the corresponding normalized change of the elastic energy stored in the contacts at the end of the loading-unloading cycle, and shows similar angle dependence as the dissipation. This change in

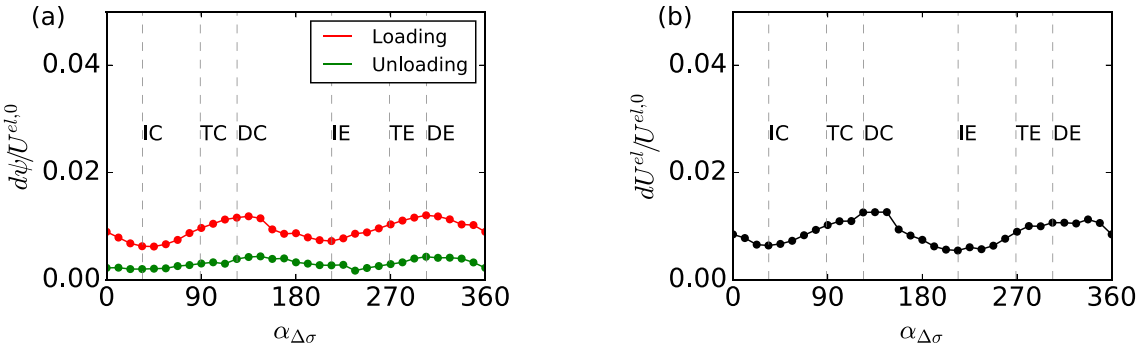

Fig. 13. a) Frictional dissipation during loading-unloading, and b) stored plastic work in a cycle, both normalized with the initial stored elastic energy, and plotted against the Rendulic angle, during probing at the *isotropic state A*.

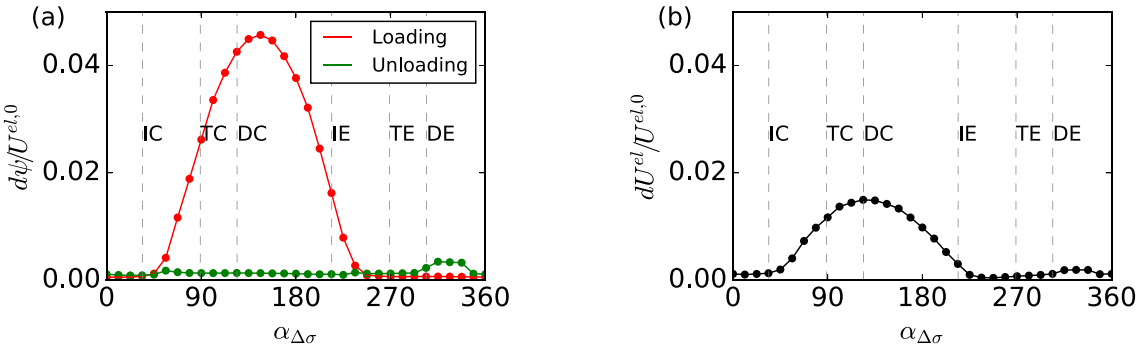

Fig. 14. a) Frictional dissipation during loading-unloading, and b) stored plastic work in a cycle, both normalized with the initial stored elastic energy, and plotted against the Rendulic angle, during probing at the *anisotropic state B*.

stored energy reflects the arrangement of contacts and corresponds to the stored plastic work (hardening) in the system. The same quantities are plotted for the anisotropic state *B* in Fig. 14. At this state, maximum dissipation occurs near (DC), while almost no dissipation occurs at (DE). During unloading, the situation is reversed, i.e. we observe most dissipation near (DE). Finally, the distribution of stored plastic work reflects processes occurring during both loading and unloading.

3.5. Micromechanics

3.5.1. Fluctuation-dissipation observations

The goal of this section is to shed light on the nature of dissipation, and reveal its relation to contact fluctuations. Radjai et al. (1998) established that, in idealized two-dimensional assemblies, full mobilization of friction predominantly occurs in the so-called weak network. Fig. 15(a) verifies this observation in our 3D granular assembly by plotting, for various probes, the rate of dissipation at each contact against the associated interparticle force. For large enough contact force magnitudes, we observe an exponential decay of dissipation with increasing contact force for all probes originating from all three initial states.

On the contrary, the relation of dissipation to contact fluctuations has not been properly investigated, despite its importance. Fig. 15(b) shows the rate of dissipation at each contact against the associated magnitude of the fluctuation in the deformation of the contact (see Eq. (E.1)), which is related to the force fluctuation via the interparticle contact law. We observe a substantial increase in the rate of dissipation with increasing fluctuation magnitude. In fact, fluctuations that are lower than a threshold - dependent on the contact scale parameters that govern the frictional limit - exhibit almost no dissipation which lends credibility to the notion of elastic fluctuations (Appendix E). This observation may be verified pictorially by inspecting Fig. 16a) and b). Fig. 16a) shows, for a two-dimensional cross-section of the dense specimen, the contact deformation fluctuation vectors during probing (computed via Eq. (E.1)), while Fig. 16b) shows the corresponding contours of frictional dissipation rate at the same instant. One can observe active regions with both pronounced frictional dissipation and large fluctuation magnitudes.

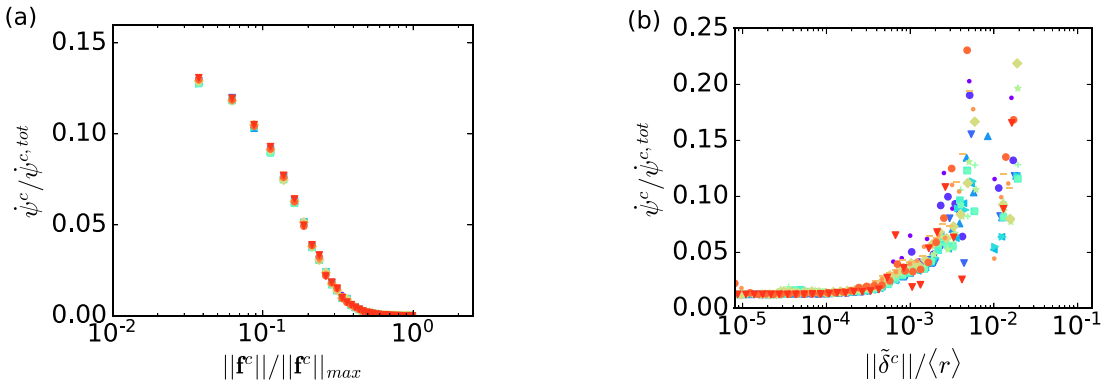

Fig. 15. Normalized dissipation versus a) normalized force magnitude, and b) normalized contact fluctuation magnitude. Colors represent different probes originating at state *A*.

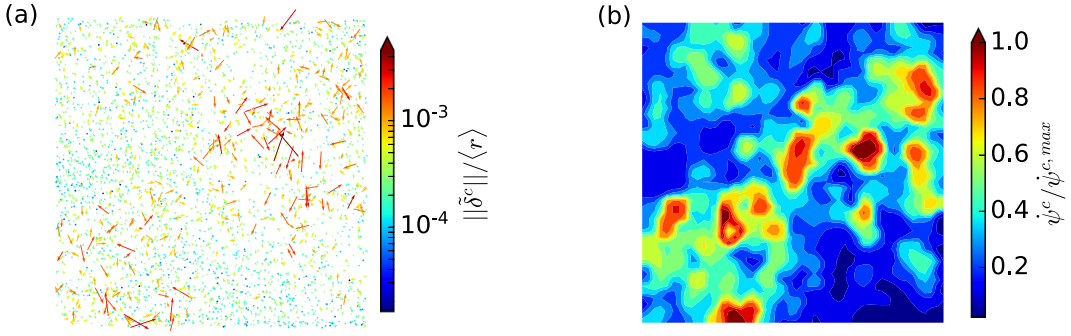

Fig. 16. Two-dimensional slices of (a) contact deformation fluctuations, (b) normalized rate of dissipation for the dense specimen.

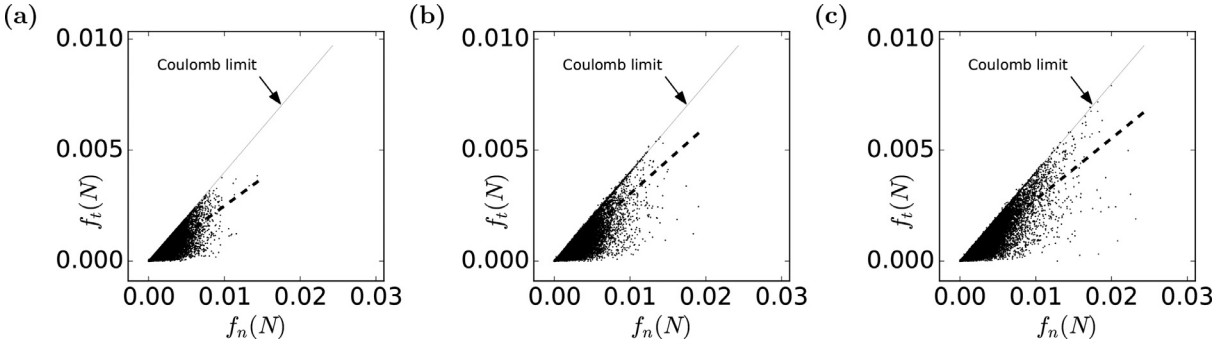

Fig. 17. Tangential vs normal contact forces for the dense granular assembly at states (a) A, (b) B and (c) B'.

3.5.2. Mobilized friction and plastic debt

The focus of this section is to describe the evolution of the micromechanical state of the sample in terms of mobilized friction at the contact scale. Fig. 17 shows the relationship between the magnitude of the tangential (f_t) and normal (f_n) contact force for all contacts in the three considered states. Their ratio represents the contact-scale mobilized friction $\eta = f_t/f_n$, bounded by the Coulomb limit, while dashed lines represent the system average. Interestingly, we identify a substantial percentage of contacts at the Coulomb limit at the isotropic state - a departure from previous observations on spheres (Calvetti et al., 2003b). Not surprisingly, the amount of sliding contacts increases in the anisotropic state *B*, to accommodate the increasing level of macroscopic shear. This is also evident by the increase in the average mobilized friction. At the preloaded state B', the magnitude of forces increases, while the mobilized friction decreases, in accordance with previous observations in spheres (Calvetti et al., 2003b).

Further information about the micromechanical state of the system can be obtained by adopting the machinery of Calvetti et al. (2003b). To this end, we introduce the scaled mobilized interparticle friction $\eta_\mu = f_t/(\mu f_n)$, noting that $\eta_\mu \leq 1$ for conventional probes, while $\eta_\mu > 1$ is possible for reversible (inhibited-dissipation) probes. In the latter, the

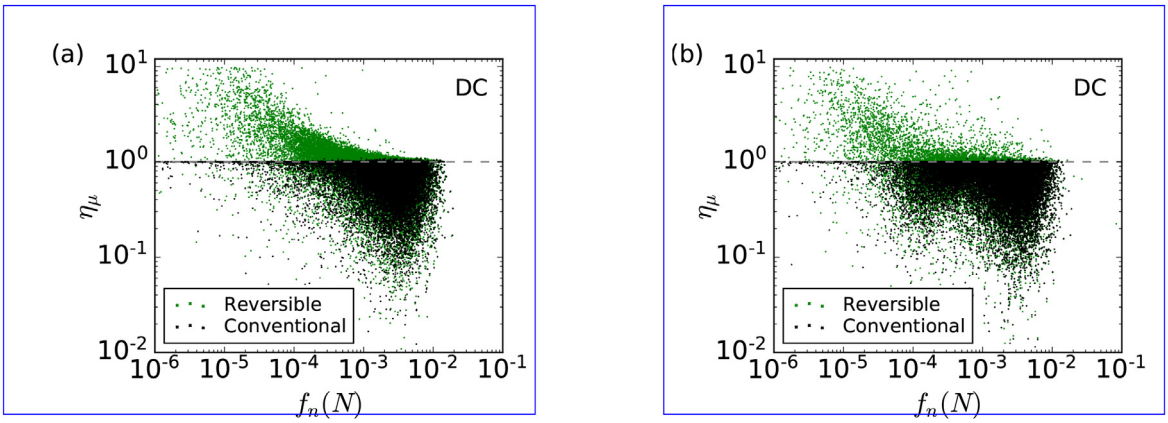

Fig. 18. Mobilized friction versus normal force for the dense granular assembly during stress probing along a) deviatoric compression (DC), and b) deviatoric extension (DE) at state *B*.

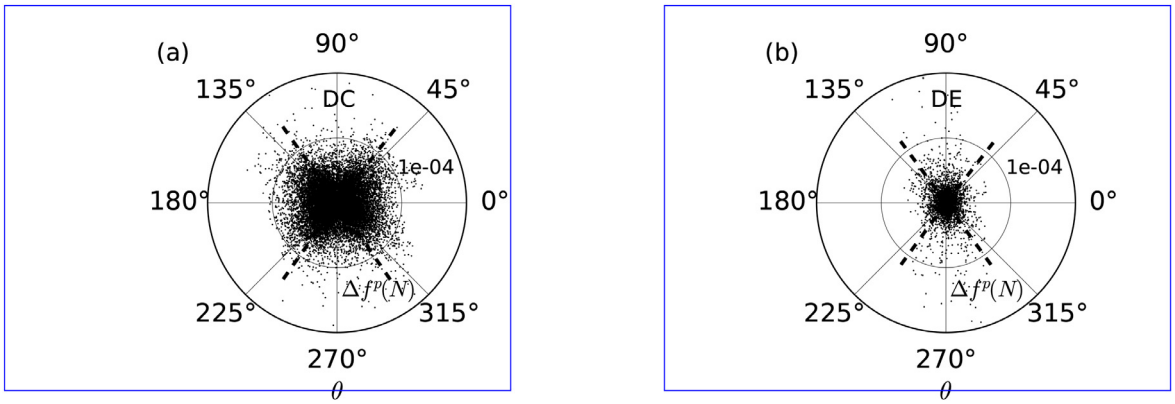

Fig. 19. Plastic debt vs contact orientation angle for the dense granular assembly during probing along a) deviatoric compression (DC), and (b) deviatoric extension (DE) at state *B*. Dashed lines represent the weighted average orientation of plastic debt at each quadrant.

quantity $\Delta f^p = f_t - \mu f_n$ is interpreted as a plastic "debt" (as defined in (Calvetti et al., 2003b)), that would be required to bring sliding contacts back to the Coulomb limit. For conciseness, we only present such measurements for two characteristic along the (DC) and (DE) directions, at state *B*. In particular, Fig. 18 shows the mobilized interparticle friction as a function of the magnitude of normal contact force, for both conventional and reversible probes. Substantial irreversible behavior emerges during the (DC) probe, which is evident by the development, in the case of the reversible probes, of shear forces larger than those allowed by the Coulomb condition. On the contrary, during the (DE) probe, only few contacts experience shear forces above the frictional limit. For the same probes, Fig. 19 reports the plastic debt against the contact orientation angle projected in the $x-z$ plane (θ), indicating some degree of preferred orientation albeit with significant scatter. This is more clearly seen by the misalignment of the weighted average orientation of plastic debt at each quadrant - represented by dashed lines - with the diagonal directions. A perfect alignment would indicate a uniform (isotropic) orientational distribution.

3.6. Fabric evolution

The change in structure revealed partially in Sections 3.4 using the isotropic measure of stored energy, and in Section 3.5.2 using the concept of plastic debt, is now further illuminated by investigating the evolution of fabric. Fig. 20 shows the evolution of different measures of fabric, during probing for the two characteristic probes (DE) and (DC) at state A. Similarly, Fig. 21 shows the fabric evolution at state B. In particular, (a1-a2) and (b1-b2) show the change in orientational distribution of contact normals that belong to the strong and weak network respectively, along a slice in the x-z plane. Green and red colors are used to mark a positive (gain) and negative (loss) change in the contact density, respectively. Further, (c1-c2) show the orientational distribution of the magnitude of contact displacement fluctuations. For both states and both probes, we observe that strong network contacts are consistently gained in the direction of compressive loading. On the other hand, the density of sliding contacts increases roughly in the perpendicular direction, and decreases in a direction almost parallel to the plastic strain direction. Interestingly, at the isotropic state *A* while probing along (DC), the sliding

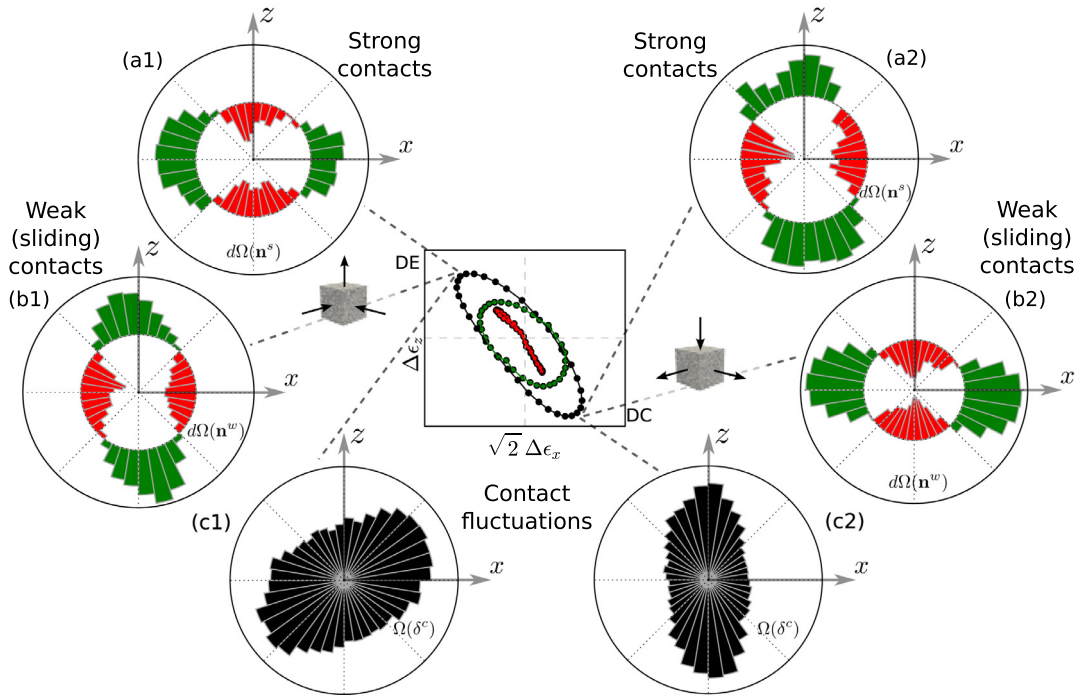

Fig. 20. Incremental change in fabric of contact normals in (a) the strong force network, and (b) and weak force network, and (c) orientational distribution of contact displacement fluctuations for probing at *state A*. Numbers denote loading path (1: DE, 2: DC).

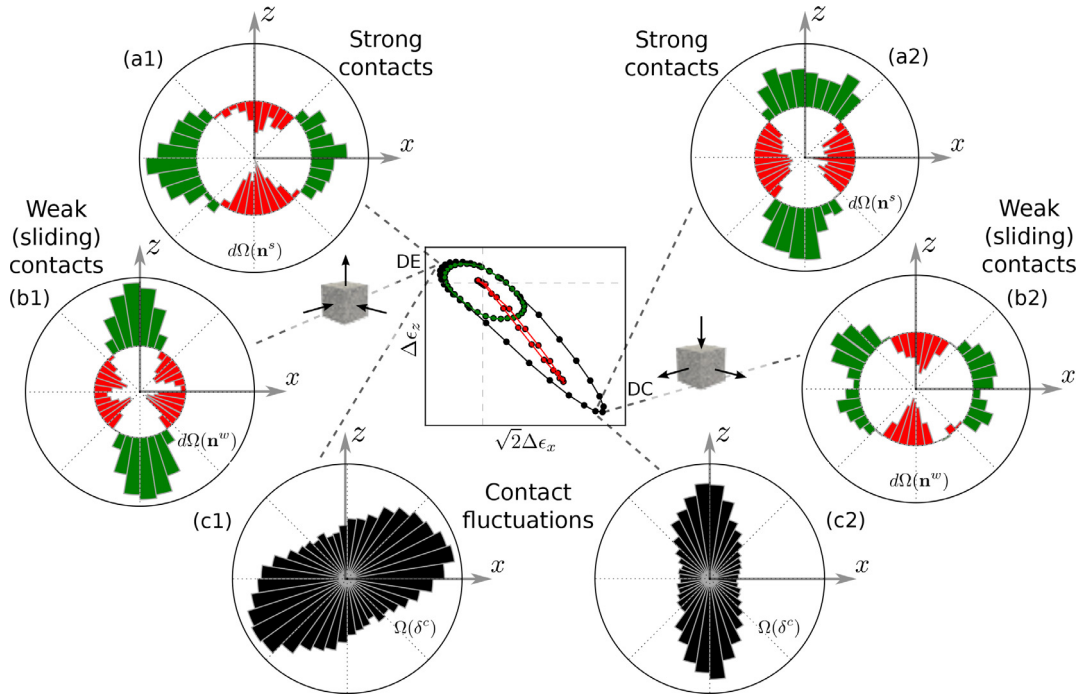

Fig. 21. Incremental change in fabric of contact normals in (a) the strong force network, and (b) and weak force network, and (c) orientational distribution of contact displacement fluctuations for probing at *state B*. Numbers denote loading path (1: DE, 2: DC).

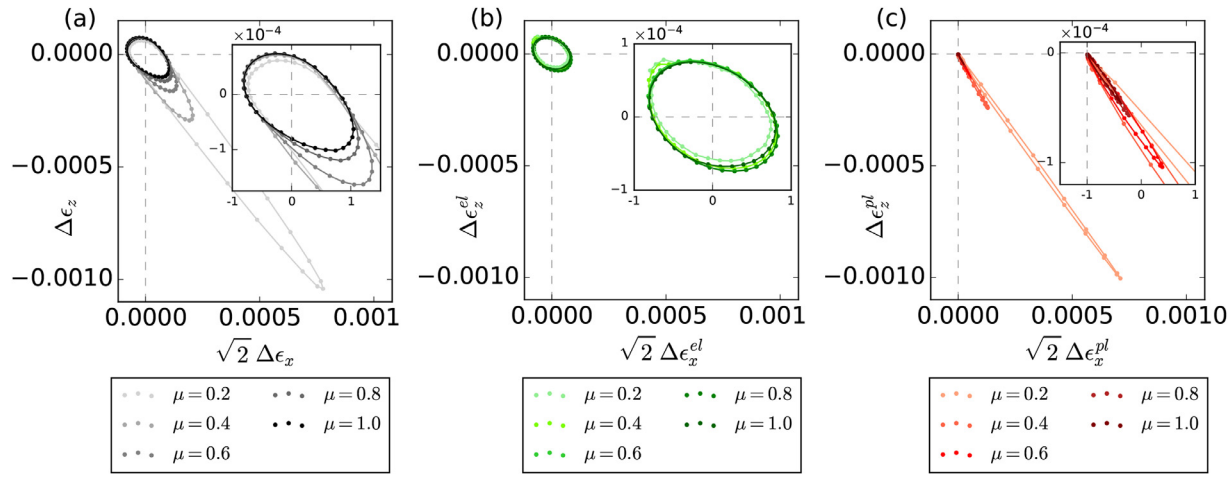

Fig. 22. (a) Total, (b) Elastic and (c) Plastic strain response envelope for the dense *granular* assembly at the anisotropic state *B* for varying interparticle friction.

contact density gain is unimodal in nature, as opposed to the bimodal gain in the case of the same probe at the anisotropic state *B*. The same modality difference is observed when comparing the sliding contact density loss for the (DE) probe at states *A* and *B*. For a related discussion on the anisotropy of the weak network in biaxial experiments, we refer to (Alonso-Marroquín et al., 2005). Finally, the orientation of maximum contact fluctuations appears to be correlated with the direction of maximum loss of sliding contacts.

3.7. Effect of interparticle friction

In this section we briefly investigate the effect of interparticle friction μ in the incremental response. Fig. 22 compares the total, elastic and plastic strain response envelopes obtained during stress probing at state *B* for a range of values $\mu \in [0.2, 1]$. We identify an anticlockwise rotation and contraction of the total and plastic strain response envelope with increasing interparticle friction. Once the latter increases beyond a critical value $\mu_{cr} \approx 0.8$, the envelopes converge to a well-defined shape, and the macroscopic response is completely dictated, at that point, by particle morphology. These observations are in line with studies showing that the macroscopic friction plateaus with increasing interparticle friction (Luding, 2005). The elastic envelopes remain essentially unaffected.

3.8. Effect of particle shape

In this section, we focus on investigating the effect of particle shape on mapping the grain-scale behavior to the incremental continuum response. In particular, we choose to address the effect of the common spherical idealization (e.g. Bardet, 1994; Calvetti et al., 2003a; Calvetti et al., 2003b; Froiio and Roux, 2010; Tamagnini et al., 2005; Wan and Pinheiro, 2013), by comparing the granular sample to an equivalent spherical one; the investigation presented in this work could serve as the backbone for a systematic study of particle morphology on the incremental continuum response of granular media. Via the same dry pluviation procedure (Section 3.1), we construct an idealized spherical counterpart of the dense granular assembly. To this end, each grain is substituted by a sphere of equal volume, while keeping particle material properties the same. Further, in order to achieve a fair comparison between the spherical and granular assembly, the same relative density ($D_r = 85\%$) is imposed[3] Note that this consideration compensates partly for shape since it accounts for its effect on $e_{\min}, e_{\max}$ (Salot et al., 2009). The latter were estimated as $e_{\min} = 0.61$ and $e_{\max} = 0.75$ respectively, following the same protocol described in Section 3.1). The granular sample and its idealized spherical counterpart are depicted in Fig. 23. The spherical specimen undergoes the same isotropic-triaxial compression history in order to achieve states *A*, *B* and *B′*, which, then, serve as initial conditions to the same stress probing protocols. Fig. 24 compares the strain response envelopes (total, elastic, plastic, reversible and irreversible) of the idealized and granular assembly at state *A*, while Figs. 25 and 26 show the same comparison at states *B* and *B′* respectively. The following observations ensue:

- The spherical assembly exhibits a similar strain response to the granular one at the isotropic state. Yet, at the anisotropic and preloaded states, the response deviates significantly.

[3] Experiments were also conducted for granular and spherical samples created at the same void ratio rather than the same relative density, during which qualitatively similar differences were observed.

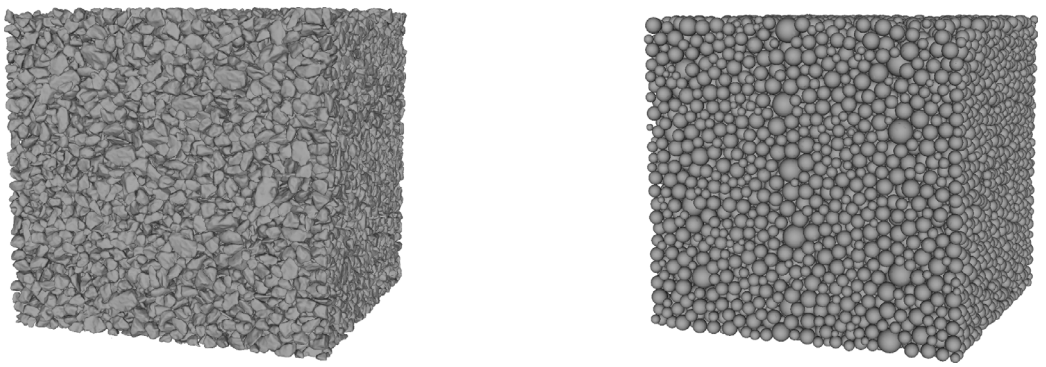

Fig. 23. Granular assembly and its idealized spherical counterpart.

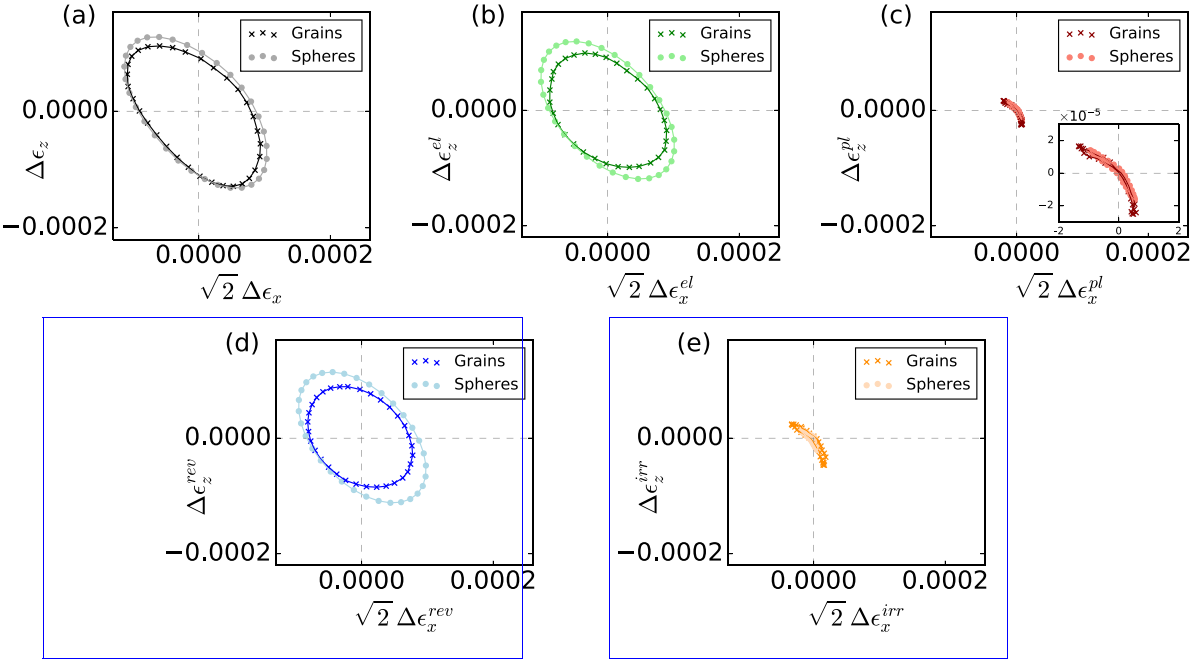

Fig. 24. (a) Total, (b) Elastic, (c) Plastic, (d) Reversible, and (e) Irreversible strain response envelope for the spherical and granular assembly at the *isotropic* state *A*.

- The spherical assembly undergoes larger plastic strains, which is consistent with observations of increasing mobilized macroscopic friction angle with increasing angularity (CEGEO et al., 2012).
- At the isotropic state *A*, the difference in strain response due to particle shape is small, which indicates reduced interlocking and mobilization of friction at that state.
- At the virgin state *B*, we observe a substantial increase in magnitude (~ 35%), and a shift in the direction of plastic flow in the case of the spherical assembly.
- Differences in macroscopic strain response are most pronounced at state B'. Plastic strains for the spherical specimen are 6 times larger than the granular specimen, while the asymmetry of the irreversible envelope of the granular assembly is also more prounced.

For completeness, Appendix F extends these macroscopic observations of shape to the grain scale, by comparing the statistics of micromechanical attributes of the two assemblies.

Remark 3. Note that the above differences in the incremental response due to particle morphology may be partially alleviated by incorporating rolling friction into the interaction between spheres, which, however, requires laborious calibration (e.g. Calvetti et al., 2003a; Plassiard et al., 2009) and does not guarantee realistic behavior beyond the calibrated stress paths.

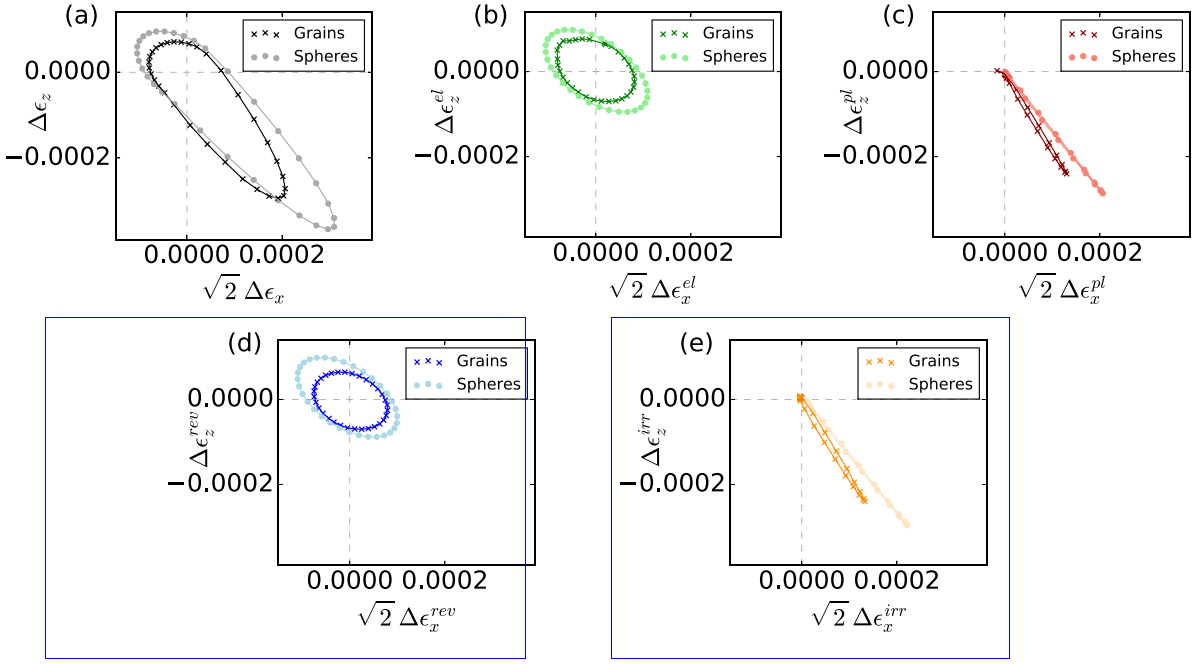

Fig. 25. (a) Total, (b) Elastic, (c) Plastic, (d) Reversible, and (e) Irreversible strain response envelope for the spherical and granular assembly at the *virgin* state B.

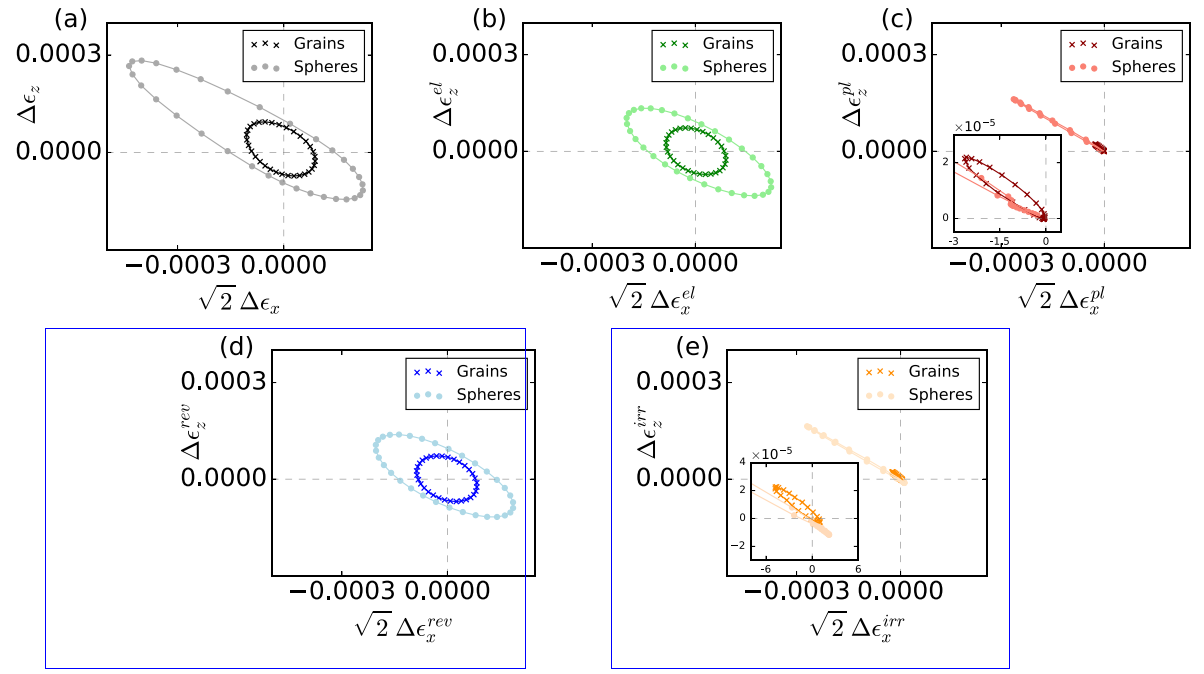

Fig. 26. (a) Total, (b) Elastic, (c) Plastic, (d) Reversible, and (e) Irreversible strain response envelope for the spherical and granular assembly at the *preloaded* state B'.

3.9. Yield surface and flow rule

The final section of this work focuses on quantifying yield and plastic flow in 3D principal stress space, which has only been investigated through physical experiments or, computationally, for idealized assemblies (Thornton, 2000). To this end, the specimen described in Section 3.1 is first subjected to isotropic compression followed by rectilinear deviatoric stress probes with uniformly distributed Lode angle. The process is repeated for deviatoric planes corresponding to multiple

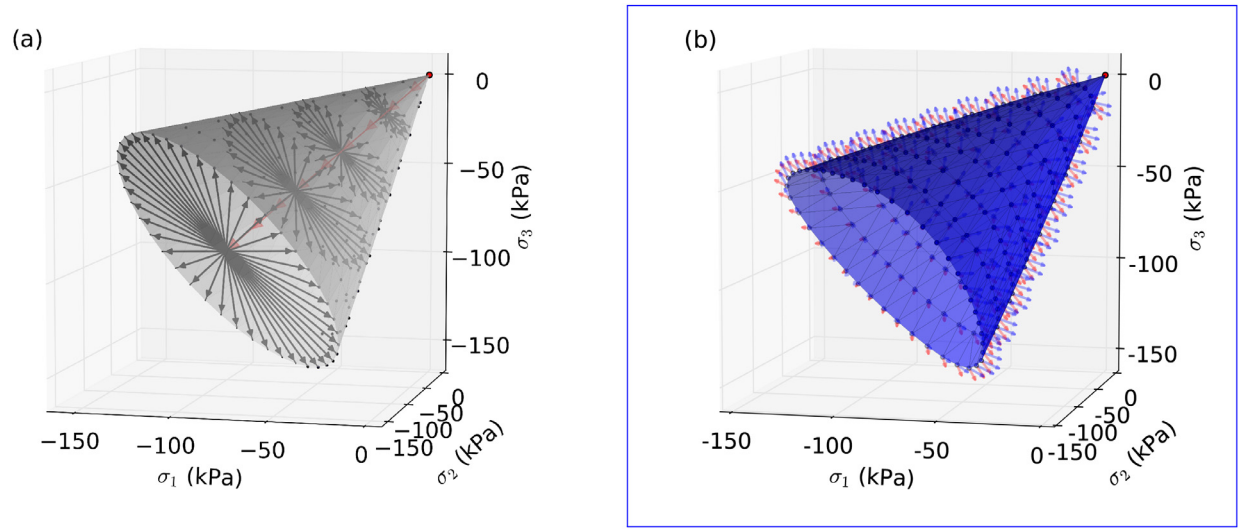

Fig. 27. (a) Rectilinear deviatoric probes, and (b) Yield surface in principal stress space with surface normals (blue arrows) and incremental plastic strain vectors (red arrows). (For interpretation of the references to colour in this figure legend, the reader is referred to the web version of this article.)

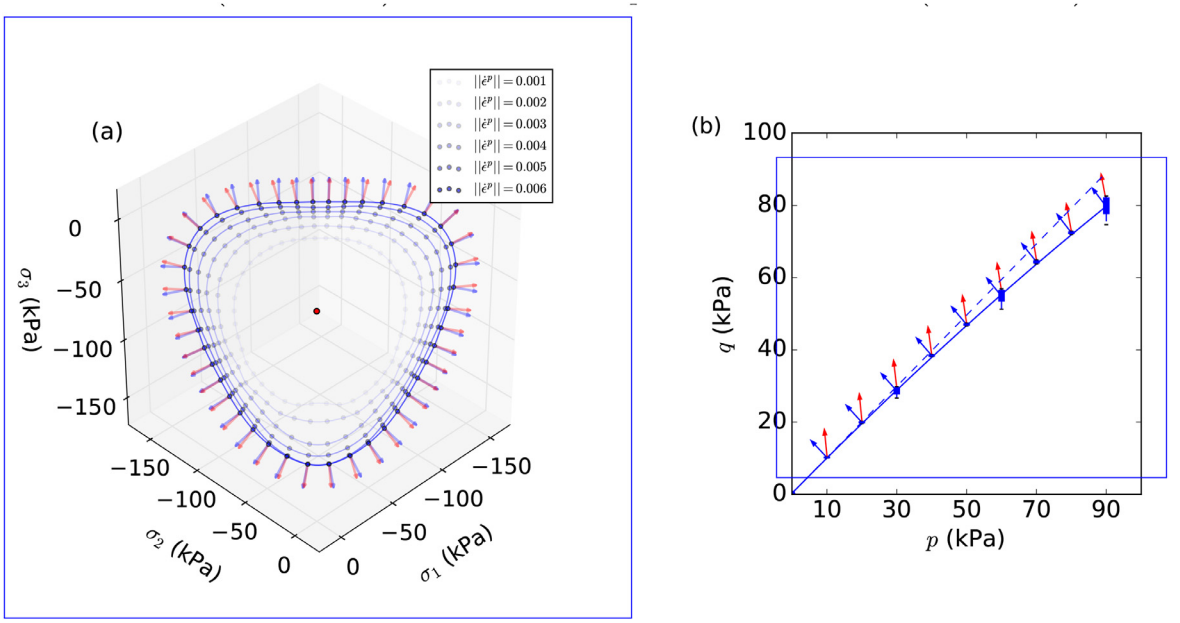

Fig. 28. (a) Deviatoric plane (p=90 kPa), and (b) Meridian plane (θ=0°).

pressure levels, until a cone is covered in the principal stress space (Fig. 27(a)). As opposed to previous studies (Calvetti et al., 2003a; Thornton, 2000) who only considered a sextant section of a deviatoric plane, here, each plane is completely covered to account for potential fabric effects. Throughout each probe, the evolution of plastic strain rate is monitored. We interpret the yield surface as the locus of stress states corresponding to the same value of the norm of plastic strain rate. We find that beyond a value of $||\dot{\boldsymbol{\epsilon}}^p|| = 5 \cdot 10^{-3}$, the surfaces essentially converge to an ultimate yield surface, which is shown in 3D in Fig. 27(b). Fig. 28(a) shows in more detail a particular deviatoric plane ($p = 90$ kPa), where the convergence of the sequence of yield surfaces is evident. In the same figure, the plastic strain increments are compared to the yield surface normals, exhibiting only minor nonassociativity (in regions of pronounced shear), verifying previous experimental and numerical observations (Anandarajah et al., 1995; Lade, 1977; Wan and Pinheiro, 2013). Further, we find that this minor degree of associativity is independent of pressure. Fig. 28(b) shows a characteristic meridian plane corresponding to Lode angle $\theta = 30^\circ$. In this plane we observe prominent nonassociativity, in accordance with previous experimental evidence that normality tends to overpredict the volumetric plastic strain. Upon closer observation, we can identify a small decrease in

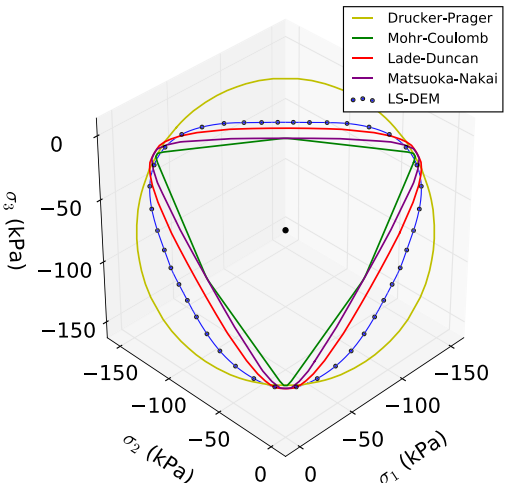

Fig. 29. Comparison of analytical yield loci with virtual experiment data.

the degree of associativity with increasing pressure. This is related to the curved nature of the yield surface, highlighted in the same figure.

Naturally, the next step is to compare these high fidelity results with common analytical yield loci. Fig. 29 compares the yield locus obtained by the experiments against the Lade and Duncan (1973) ($I_1^3 - bI_3 = 0$), Mohr-Coulomb ($|\sigma_i - \sigma_j|/(2\sqrt{\sigma_i\sigma_j}) - \tan\phi = 0$), Drucker and Prager (1952) ($I_1 - aJ_2 = 0$) and Matsuoka and Nakai (1974) ($I_1 I_2 - cI_3 = 0$) loci, where I_1, I_2, I_3 are the first, second and third stress invariants, and J_2 is the second deviatoric stress invariant. The macroscopic friction angle under compression was calibrated for the Mohr-Coulomb criterion at $\phi \approx 51^\circ$. Then the following expressions produce the parameters that are consistent with the Mohr-Coulomb criterion:

$$a = \frac{2\sin\phi}{\sqrt{3}(3-\sin\phi)} \quad b = \frac{(3-\sin\phi)^3}{\cos^2\phi(1-\sin\phi)} \quad c = \frac{9-\sin^2\phi}{1-\sin^2\phi}$$

For each of the criteria, we calculate the average pressure-normalized ℓ_2 error measure, given by $e = 1/(pN)\sum_{i=1}^{N} ||\boldsymbol{\sigma}_i^{\text{LS-DEM}} - \boldsymbol{\sigma}_i^{\text{Model}}||_2$, where $\boldsymbol{\sigma}_i^{\text{LS-DEM}}, \boldsymbol{\sigma}_i^{\text{Model}}$ are the stress states corresponding to the virtual experiment and particular model respectively, at the ith point of the discretized yield surface comprised of a total of N points. We obtain:

Model	Drucker-Prager	Mohr-Coulomb	Lade-Duncan	Matsuoka-Nakai
Error (e)	0.137	0.095	0.040	0.076

Among the available loci, the ultimate yield surface is best described by the Lade-Duncan one.

4. Conclusions

We have presented an *in silico* experimentation framework for granular materials, enabled by the accurate mathematical representation of the morphology and interaction of particles, as well as the control of their collective state, far beyond what has been accessible with preexisting techniques. Naturally arising, within this new paradigm, is the concept of a granular 'DNA' and its expression to an emergent macroscopic behavior that is largely free from idealizations. The remainder of the paper focused on utilizing virtual stress probing experiments towards a systematic investigation of the incremental behavior of sand.

In a first set of axisymmetric experiments, we quantified the reversible (i.e. those due to dissipation-free grain-scale mechanisms) and the elastic strains (i.e. those recovered upon unloading) in the granular assembly due to axisymmetric probing. We found that the reversible strain envelopes are slightly smaller (and, hence, contained within) the elastic ones, and quantified the anisotropy in the elastic response. In accordance with previous works, we identified evidence of a nonassociative and slightly nonregular flow rule. Next, we provided quantitative measurements of energy dissipation and contact fluctuations, the decoding of which remains the cornerstone of granular mechanics, and exhibited a threshold 'elastic' fluctuation above which the onset of yielding occurs. Finally, hardening processes were examined from the perspective of the evolution of stored plastic work and fabric in the strong and weak contact networks.

Subsequent experiments focused on quantifying the effect of particle friction and morphology on the macroscopic response. Regarding the former, a combined effect of rotation and contraction of the strain response envelopes was identified upon increase of the interparticle friction. Beyond a critical value, the envelopes converge to a stationary envelope dictated by particle morphology. Remarkably, the idealized spherical counterpart of a granular assembly could qualitatively capture

almost all aspects of its incremental behavior. Yet, from a quantitative perspective, we identified an important signature of morphology at anisotropic and, in particular, preloaded states. More specifically, experiments revealed a larger magnitude of plastic strain and a less pronounced stiffness increase due to preloading in the spherical specimen compared to the actual granular specimen.

A last set of deviatoric stress probing experiments furnished an important application of the proposed framework, where the entire yield surface and plastic potential was mapped in 3D principal stress space. We investigated the influence of pressure and Lode angle on the nonassociativity of the plastic flow, and found that, among the common analytical criteria, the failure surface was best described by the Lade-Duncan criterion.

The evidence from this study highlights the importance of high fidelity characterization and virtual testing for sands and potentially many other particulate materials. We are confident that such findings will help expand our understanding of the behavior of granular materials, and eventually guide the development of a new generation of constitutive theories. Interesting future avenues involve more in-depth investigation of granular fabric as well as the incorporation of grain fracture and multiphysics coupling. Finally, we see great potential in using virtual experiments to create a high-fidelity database for different families of granular materials, to be leveraged by data-driven and machine learning techniques.

Declaration of Competing Interest

The authors declare that they have no known competing financial interests or personal relationships that could have appeared to influence the work reported in this paper.

Acknowledgements

The authors would like to acknowledge the detailed analysis of this work by the two anonymous reviewers, which has contributed to its substantial improvement. Their feedback is gratefully appreciated.

Appendix A. Thermodynamical description of contact interaction

Presented here is a standard thermodynamic formalism of the discrete contact interaction problem. In analogy to continuum thermodynamics (Ortiz, 2012; Ziegler, 1977), consider the Gibbs energy G^c at a contact:

$$G^c = G^c(\mathbf{f}^c, \mathbf{q}^c, \theta) \tag{A.1}$$

as a function of the contact force $\mathbf{f}^c$, the temperature θ and an internal variable $\mathbf{q}^c$ related to dissipative events (e.g. sliding). Neglecting thermal effects, the free energy vanishes at zero interparticle force. A convenient way to formulate the energy is through the local compliance $\mathbf{C}^c$ at the contact:

$$G^c = -\frac{1}{2}\mathbf{f}^c \cdot \mathbf{C}^c\mathbf{f}^c - \mathbf{f}^c \cdot \mathbf{q}^c \tag{A.2}$$

By construction, the internal variable $\mathbf{q}^c$ represents the plastic deformation $\boldsymbol{\delta}^{c,\mathrm{p}}$ that remains at the contact upon unloading to zero force,

$$\mathbf{q}^c = -\frac{\partial G^c}{\partial \mathbf{f}^c}\bigg|_{\mathbf{f}^c=\mathbf{0}} =: \boldsymbol{\delta}^{c,\mathrm{p}} \tag{A.3}$$

The decomposition of the contact deformation into an elastic and plastic part follows by duality:

$$\boldsymbol{\delta}^c = -\frac{\partial G^c}{\partial \mathbf{f}^c} = \boldsymbol{\delta}^{c,\mathrm{e}} + \boldsymbol{\delta}^{c,\mathrm{p}} \tag{A.4}$$

where:

$$\boldsymbol{\delta}^{c,\mathrm{e}} = \mathbf{C}^c\mathbf{f}^c \quad \text{or} \quad \mathbf{f}^c = \mathbf{C}^{c^{-1}}\boldsymbol{\delta}^{c,\mathrm{e}} = \mathbf{K}^c\boldsymbol{\delta}^{c,\mathrm{e}} \tag{A.5}$$

where $\mathbf{K}^c$ is the inverse compliance (stiffness) at the contact.

Assuming Ziegler's orthogonality condition, the dissipative force conjugate to the internal variable is given by:

$$\boldsymbol{\chi}^c = \frac{\partial G^c}{\partial \boldsymbol{\delta}^{c,\mathrm{p}}} = \mathbf{f}^c \tag{A.6}$$

Note in passing that the contact compliance is assumed to be independent of internal processes ($\mathbf{q}^c$), for the sake of simplicity. Generalization towards contact damage or aging (Sadrekarimi and Olson, 2010) is easily achieved by dropping this assumption. In order to obtain a closed set of equations, the above equilibrium relations need to be combined with appropriate kinetic relations (Ortiz, 2012). Indeed, the existence of a kinetic (dissipation) potential ψ^c follows from standard thermodynamic arguments (Onsager, 1931) such that:

$$\dot{\boldsymbol{\delta}}^{c,p} \in \partial_{\boldsymbol{\chi}^c}\psi^c \tag{A.7}$$

In an algorithmic (incremental) setting, we obtain the equivalent relations:

$$d\boldsymbol{\delta}^c = d\boldsymbol{\delta}^{c,\mathrm{e}} + d\boldsymbol{\delta}^{c,\mathrm{p}} \tag{A.8}$$

$$d\mathbf{f}^c = \mathbf{K}^c d\boldsymbol{\delta}^{c,\mathrm{e}} \tag{A.9}$$

$$d\boldsymbol{\delta}^{c,p} \in \partial_{\boldsymbol{\chi}^c} \psi^c \tag{A.10}$$

Finally, to fully determine the contact law, a specific form of the contact stiffness and the kinetic potential needs to be identified. The prototypical example, used in the stress probing experiments of Section 3, is that of a Hookean stiffness with Coulomb friction. In this case, the contact stiffness is given by:

$$\mathbf{K}^c = \mathbf{C}^{-1} = k_n^c\, \mathbf{n}^c \otimes \mathbf{n}^c + k_t^c\, (\mathbf{s}^c \otimes \mathbf{s}^c + \mathbf{t}^c \otimes \mathbf{t}^c) \tag{A.11}$$

where $(\mathbf{n}^c, \mathbf{s}^c, \mathbf{t}^c)$ form a local cartesian system at the contact c, and k_n^c, k_t^c are the normal and tangential stiffness respectively (Agnolin and Roux, 2007b), while the kinetic potential is given by the indicator function $I_{\mathcal{C}}(\mathbf{f}^c)$ of the Coulomb cone $\mathcal{C}$:

$$\mathcal{C} = \{\mathbf{f}^c \,|\, ||\mathbf{f}^c - (\mathbf{f}^c \cdot \mathbf{n}^c)\mathbf{n}^c|| - \mu(\mathbf{f}^c \cdot \mathbf{n}^c) \leq 0\} \tag{A.12}$$

where $\mathbf{n}^c$ denotes the contact normal, and μ the interparticle friction.

Remark 4. The thermodynamic description provided herein is far from general. Instead, the contact scale interaction is treated as 'standard' material behavior, which includes a specific form of the Gibbs free energy and the restrictive statement of Ziegler's orthogonality. As a result, complex interaction laws such as frictional Hertzian contact cannot be captured by the framework in its current form. For a more general discussion of thermodynamic modeling applied to the continuum behavior of frictional materials, the interested reader is referred to (Collins and Houlsby, 1997).

Appendix B. Effect of the size of the RVE

We verify the representativeness of the granular assembly through a simple investigation of the effect of sample size. Four samples of the same relative density ($D_r = 85\%$) were constructed, that comprised of an increasing number of grains (4913, 9261, 15,625 and 19,683 respectively). The samples were subjected to drained triaxial compression to the anisotropic state B, followed by an axisymmetric stress probing protocol (Section 3.1). We observe satisfactory convergence of the strain response to a well defined envelope for sample sizes above 15,625 grains (Fig. B.30).

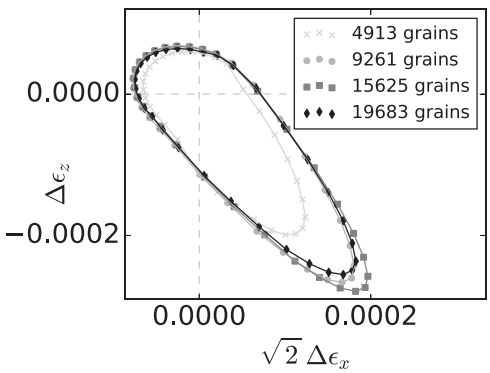

Fig. B.30. Effect of sample size on the strain response envelope.

Appendix C. Irreversibility of contact deformation during unloading

We provide evidence of the irreversibility of contact deformation upon unloading, similarly to a recent investigation by Kuhn and Daouadji (2018). To do so, we track the contacts that were sliding during loading for a probing experiment at state B. In particular, Fig. C.31 shows the transition of the number of such sliding contacts N^c, normalized by the number of particles N^p, upon unloading for various probing directions. We observe that a significant proportion of sliding contacts continue to slide during unloading, regardless of the direction of probing. This evidence suggests that contact deformations are not reversed during unloading.

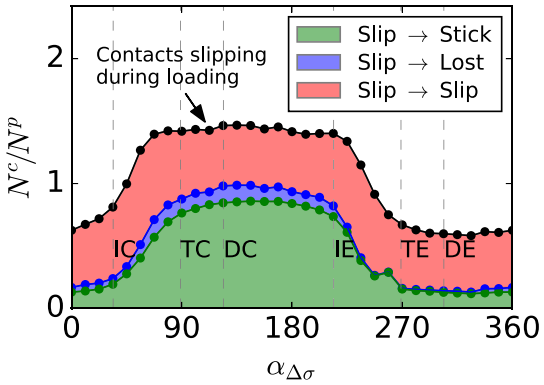

Fig. C.31. Transition of number of contacts, normalized by number of particles, that were sliding during loading, plotted as a function of the probing angle.

Appendix D. Calculation of elasticity parameters

We address the calculation of elasticity parameters in Table 2. First, a least-squares fit is applied to solve for the components of the elastic stiffness tensor $\mathbf{C}$ (in the principal plane) below:

$$\begin{bmatrix}\Delta\sigma_x\\ \Delta\sigma_y\\ \Delta\sigma_z\end{bmatrix} = \begin{bmatrix}C_{11} & C_{12} & C_{13}\\ C_{21} & C_{22} & C_{23}\\ C_{31} & C_{32} & C_{33}\end{bmatrix}\begin{bmatrix}\Delta\epsilon_x\\ \Delta\epsilon_y\\ \Delta\epsilon_z\end{bmatrix} \tag{D.1}$$

given the data pairs ($\Delta\boldsymbol{\sigma}$, $\Delta\boldsymbol{\epsilon}$) for all probes at a specific state. By comparing the fitted stiffness tensor $\mathbf{C}$, to the isotropic and transversely isotropic elasticity tensors:

$$\mathbf{C}^{iso} = \begin{bmatrix}1/E & -\nu/E & -\nu/E\\ -\nu/E & 1/E & -\nu/E\\ -\nu/E & -\nu/E & 1/E\end{bmatrix} \qquad \mathbf{C}^{trans} = \begin{bmatrix}1/E_x & -\nu_x/E_x & -\nu_{zx}/E_z\\ -\nu_x/E_x & 1/E_x & C_{23}\\ -\nu_{zx}/E_z & C_{32} & 1/E_z\end{bmatrix} \tag{D.2}$$

we obtain the Young's modulus E and Poisson's ratio ν, in the case of isotropy, as well as the transverse and longitudinal moduli E_x, E_z, and the associated Poisson's ratios $\nu_x(=\nu_{xy}=\nu_{yx})$, ν_{zx}, in the case of transverse isotropy.

Appendix E. Reversible strain response

We discuss alternative strategies for extracting the reversible strain response of an assembly. As outlined in Section 3.3, by carrying out probes where frictional dissipation has been inhibited, we obtain slightly overestimated reversible strain envelopes, due to the relaxation of the contact topology. Here we compare these envelopes to those produced by two alternative strategies: i) the inhibited-dissipation/rotation approach of Calvetti et al. (2003a), and ii) an analytical homogenization-based approach.

The first method delivers the reversible response through a set of probes where we inhibit not only frictional dissipation but also grain rotation (Calvetti et al., 2003a). This additional constraint is introduced in order to preserve the contact topology, yielding a purely reversible process. However, constraining rotations has the undesired side-effect of stiffening (underestimating) the reversible response, producing a loose lower bound for the true reversible strain response. Further, rotational constraints induce external moments on the particles, which lead to the development of couple stress. The latter is known to affect the development of RVE-scale and meso-scale instabilities (Oda and Iwashita, 2000), and, hence, the determination of the true material response. The second method, detailed in the next section, extracts the reversible strain component by relying on an analytical homogenization technique and a new closure relation, that extend previous results on idealized elastic assemblies.

Fig. E.32 compares the reversible response furnished by the inhibited dissipation approach (Section 3.3.2) to that of the inhibited dissipation/rotation approach as well as the homogenization-based method, for states A, B and B' considered in this study. The last two methods give very similar results, and tend to equally underestimate the response, particularly in the (DC) and (DE) directions.

Homogenization-based approach

We derive a micromechanical expression for the decomposed reversible and irreversible strains in an assembly. To this end, consider an RVE of arbitrarily shaped particles, which is subject to an average strain increment $d\bar{\boldsymbol{\varepsilon}}$ and, thus, develops a stress increment $d\bar{\boldsymbol{\sigma}}$. At any contact c within the assembly (Fig. E.33) (between particles p, q), the displacement $d\boldsymbol{\delta}^c$ can be described (Liao et al., 1997) by a projection of the average displacement gradient $d\bar{\boldsymbol{\varepsilon}}$ to the branch vector $\mathbf{l}^c$, corrected by a nonaffine displacement fluctuation. In all generality :

$$d\boldsymbol{\delta}^c = d\bar{\boldsymbol{\varepsilon}}\cdot\mathbf{l}^c + d\tilde{\boldsymbol{\delta}}^c \tag{E.1}$$

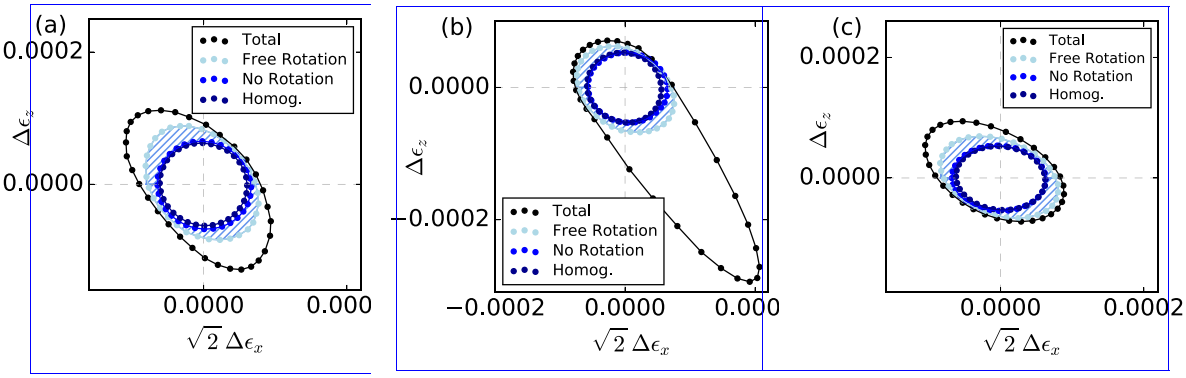

Fig. E.32. Comparison between reversible envelopes generated via free-rotation (light blue) and constrained-rotation (blue) simulations, as well as via homogenization-based approach (dark blue) for (a) the isotropic state *A*, (b) the anisotropic state *B* and (c) the preloaded state *B′*. (For interpretation of the references to colour in this figure legend, the reader is referred to the web version of this article.)

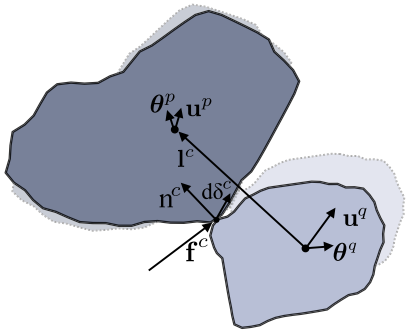

Fig. E.33. 2D schematic of deformed particle contact.

where $\mathbf{l}^c$ is the contact branch vector, and $d\tilde{\boldsymbol{\delta}}^c$ is the fluctuation of the incremental contact deformation. Invoking the decomposition of the contact deformation (Eq. (A.8)), we obtain:

$$d\boldsymbol{\delta}^{c,\mathrm{e}} + d\boldsymbol{\delta}^{c,\mathrm{p}} = d\bar{\boldsymbol{\varepsilon}} \cdot \mathbf{l}^c + d\tilde{\boldsymbol{\delta}}^c \tag{E.2}$$

We shall decompose the strain into a reversible and irreversible part:

$$d\bar{\boldsymbol{\varepsilon}} = d\bar{\boldsymbol{\varepsilon}}^{\mathrm{rev}} + d\bar{\boldsymbol{\varepsilon}}^{\mathrm{irr}} \tag{E.3}$$

Remark 5. The total strain may be directly computed based on particle kinematics (Bagi, 2006), but this is not true for its decomposition. By construction, the reversible component represents the strain derived from reversible grain-scale processes, which coincide with elastic processes at that scale.

The reversible strain will be used to define elastic contact displacement fluctuations $d\tilde{\boldsymbol{\delta}}^{c,\mathrm{e}}$ below:

$$d\boldsymbol{\delta}^{c,\mathrm{e}} = d\bar{\boldsymbol{\varepsilon}}^{\mathrm{rev}} \cdot \mathbf{l}^c + d\tilde{\boldsymbol{\delta}}^{c,\mathrm{e}} \tag{E.4}$$

In analogy with previous analytical studies of purely elastic assemblies (e.g. (Misra and Chang, 1993)), the elastic fluctuations in Eq. (E.4) are unknown, which calls for a closure relation, relating those to the average strain. This relation is furnished, in this study, by the incremental force balance of all particles in the assembly. For a particle p sharing contacts $\mathcal{C}^p$ with its neighbors, we can write:

$$\sum_{c\in\mathcal{C}^p} d\mathbf{f}^c = 0 \tag{E.5}$$

$$\sum_{c\in\mathcal{C}^p} \mathbf{K}^c d\boldsymbol{\delta}^{c,\mathrm{e}} = 0 \qquad \text{(via Eq. (A.9))} \tag{E.6}$$

$$\sum_{c\in\mathcal{C}^p} \mathbf{K}^c (d\bar{\boldsymbol{\varepsilon}}^{\mathrm{rev}} \mathbf{l}^c + d\tilde{\boldsymbol{\delta}}^{c,\mathrm{e}}) = 0 \qquad \text{(via Eq. (E.4))} \tag{E.7}$$

where $\mathbf{K}^c$ is the contact stiffness given by Eq. (A.11).

The linear system obtained by collecting the equilibrium equations for all particles is generally underdetermined (depending on the coordination number) and, therefore, needs to be supplemented by appropriate 'boundary conditions'. Consider the equilibrium of each of the two participating particles (p, q), assuming that i) contact c experiences an unknown fluctuation $d\tilde{\boldsymbol{\delta}}^{\mathrm{c,e}}$, and ii) the first shell of contacts (i.e contacts between any of the participating particles (p, q) and their neighbours ($\mathcal{C}^p, \mathcal{C}^q$ respectively)) undergo a different unknown fluctuation $d\hat{\tilde{\boldsymbol{\delta}}}^{\mathrm{c,e}}$. This simplifies the equilibrium equation of the two participating particles to a solvable system:

$$\sum_{c'\in\mathcal{C}^p\setminus c}\mathbf{K}^{c'}(d\bar{\boldsymbol{\varepsilon}}^{\mathrm{rev}}\mathbf{l}^{c'}+d\hat{\tilde{\boldsymbol{\delta}}}^{\mathrm{c,e}})+\mathbf{K}^c(d\bar{\boldsymbol{\varepsilon}}^{\mathrm{rev}}\mathbf{l}^c+d\tilde{\boldsymbol{\delta}}^{\mathrm{c,e}})=0 \tag{E.8}$$

$$\sum_{c'\in\mathcal{C}^q\setminus c}\mathbf{K}^{c'}(d\bar{\boldsymbol{\varepsilon}}^{\mathrm{rev}}\mathbf{l}^{c'}+d\hat{\tilde{\boldsymbol{\delta}}}^{\mathrm{c,e}})+\mathbf{K}^c(-d\bar{\boldsymbol{\varepsilon}}^{\mathrm{rev}}\mathbf{l}^c-d\tilde{\boldsymbol{\delta}}^{\mathrm{c,e}})=0 \tag{E.9}$$

where the sign change is due to change of reference ($\mathbf{l}^{pq}=\mathbf{l}^c=-\mathbf{l}^{qp}$). Solving Eq. (E.8) for $d\hat{\tilde{\boldsymbol{\delta}}}^{\mathrm{c,e}}$ and substituting into Eq. (E.9), we finally obtain, after algebraic manipulations:

$$d\tilde{\boldsymbol{\delta}}^{\mathrm{c,e}}=-\boldsymbol{\Gamma}^c\cdot d\bar{\boldsymbol{\varepsilon}}^{\mathrm{rev}} \tag{E.10}$$

in terms of the fluctuation tensor:

$$\boldsymbol{\Gamma}^c=\Big[\big(\mathbf{I}+\boldsymbol{\Delta}\big)\cdot\mathbf{K}^c\Big]^{-1}\cdot\Big[\sum_{c'\in\mathcal{C}^p}\mathbf{K}^{c'}\otimes\mathbf{l}^{c'}-\boldsymbol{\Delta}\cdot\sum_{c'\in\mathcal{C}^q}\mathbf{K}^{c'}\otimes\mathbf{l}^{c'}\Big] \tag{E.11}$$

and where:

$$\boldsymbol{\Delta}=\Big(\sum_{c'\in\mathcal{C}^p\setminus c}\mathbf{K}^{c'}\Big)\Big(\sum_{c'\in\mathcal{C}^q\setminus c}\mathbf{K}^{c'}\Big)^{-1} \tag{E.12}$$

Combining Eqs. (E.10) and (E.4), we can solve for the elastic contact displacement:

$$d\boldsymbol{\delta}^{\mathrm{c,e}}=d\bar{\boldsymbol{\varepsilon}}^{\mathrm{rev}}\cdot\mathbf{l}^c-\boldsymbol{\Gamma}^c:d\bar{\boldsymbol{\varepsilon}}^{\mathrm{rev}} \tag{E.13}$$

The final ingredient required here is the incremental version of the well-established virial stress relation (Bagi, 1996; Christoffersen et al., 1981):

$$d\bar{\boldsymbol{\sigma}}=\frac{1}{V}\sum_{c\in\mathcal{C}}(d\mathbf{f}^c\otimes\mathbf{l}^c+\mathbf{f}^c\otimes d\mathbf{l}^c) \tag{E.14}$$

Rearranging Eq. (E.14), and using Eq. (A.9):

$$\frac{1}{V}\sum_{c\in\mathcal{C}}\mathbf{K}^c d\boldsymbol{\delta}^{c,\mathrm{e}}\otimes\mathbf{l}^c=d\bar{\boldsymbol{\sigma}}-\frac{1}{V}\sum_{c\in\mathcal{C}}\mathbf{f}^c\otimes d\mathbf{l}^c=:d\bar{\boldsymbol{\sigma}}^{\mathrm{kt}} \tag{E.15}$$

where the RHS represents the readily computable kinetic contribution to the stress increment.

The extraction of the reversible strain is concluded by substituting for Eq. (E.13) above, to obtain:

$$\frac{1}{V}\sum_{c\in\mathcal{C}}\mathbf{K}^c(d\bar{\boldsymbol{\varepsilon}}^{\mathrm{rev}}\cdot\mathbf{l}^c-\boldsymbol{\Gamma}^c:d\bar{\boldsymbol{\varepsilon}}^{\mathrm{rev}})\otimes\mathbf{l}^c=d\bar{\boldsymbol{\sigma}}^{\mathrm{kt}} \tag{E.16}$$

or:

$$d\bar{\boldsymbol{\varepsilon}}^{\mathrm{rev}}=\Big[\frac{1}{V}\sum_{c\in\mathcal{C}}\big(\mathbf{l}^c\otimes\mathbf{K}^c\otimes\mathbf{l}^c-\mathbf{l}^c\otimes\mathbf{K}^c\cdot\boldsymbol{\Gamma}^c\big)\Big]^{-1}d\bar{\boldsymbol{\sigma}}^{\mathrm{kt}} \tag{E.17}$$

Note that the RHS solely involves micromechanical quantities readily available in a virtual experiment. Finally, the irreversible strain follows from Eq. (E.3) as $d\bar{\boldsymbol{\varepsilon}}^{\mathrm{irr}}=d\bar{\boldsymbol{\varepsilon}}-d\bar{\boldsymbol{\varepsilon}}^{\mathrm{rev}}$.

Remark 6. Not surprisingly this approach leads to the development of a 'nonaffine' stiffness tensor (Eq. (E.17)). It is similar in nature to the approach of Froiio and Roux (2010) who explicitly construct the stiffness of a disk assembly by adopting (Agnolin and Roux, 2007b), and also intimately related to previous studies, outside the context of stress probing, that deal with the analytical determination of the stiffness of an assembly of particles (Agnolin and Roux, 2007a; 2007b; 2008; Chang and Hicher, 2005; Chang et al., 1992; 1992; Emeriault et al., 1996; Jenkins et al., 2005; Jenkins and Koenders, 2004; Liao et al., 1997; Misra and Chang, 1993; Nicot et al., 2005; Ragione, 2016; Tordesillas and Muthuswamy, 2008; Walsh et al., 2007), most prominently the approach of Misra and Chang (1993), in the idealized setting and with a different closure relation.

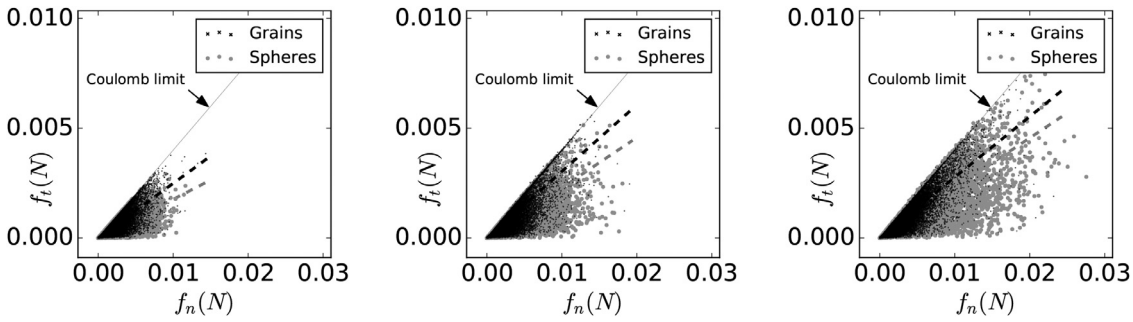

Fig. F.34. Tangential vs normal contact forces at states (a) A, (b) B and (c) B' for the granular and spherical assembly.

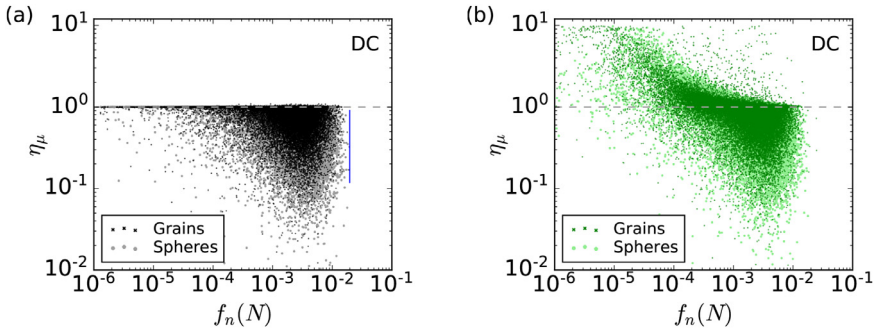

Fig. F.35. Mobilized friction vs magnitude of normal contact force for the granular and spherical assembly at the (DC) direction at state *B* for (a) the conventional, and (b) the reversible (inhibited dissipation) simulation.

Appendix F. Micromechanics of grains vs spheres

We extend here the macroscopic investigation of the influence of shape, given in Section 3.8, to the grain scale. This is achieved by comparing micromechanical attributes of the granular assembly to those of its idealized spherical counterpart. In particular, Fig. F.34 plots the tangential contact force f_t as a function of the normal force f_n for the three investigated states (A, B, B'), with the dashed lines representing the average mobilized friction angles. Interestingly, the granular assembly consistently exhibits a higher mobilization of interparticle friction at any given state, while the distribution of forces of the two samples is qualitatively similar. Analogous observations can be made by inspecting Fig. F.35 which compares the mobilized friction angle of the two assemblies plotted against the magnitude of normal force for the conventional and reversible (DC) probes at state B. Beyond the clear qualitative agreement, we verify the emergence of a higher mobilized interparticle friction for the granular assembly in the conventional probes. Measurements taken at different states and stress paths led to the same conclusions, and were thus omitted in this comparison.

References

Agnolin, I., Roux, J.-N., 2007. Internal states of model isotropic granular packings. I. Assembling process, geometry, and contact networks. Phys. Rev. E 76, 061302. doi:10.1103/PhysRevE.76.061302.

Agnolin, I., Roux, J.-N., 2007. Internal states of model isotropic granular packings. III. Elastic properties. Phys. Rev. E 76, 061304. doi:10.1103/PhysRevE.76.061304.

Agnolin, I., Roux, J.-N., 2008. On the elastic moduli of three-dimensional assemblies of spheres: characterization and modeling of fluctuations in the particle displacement and rotation. Int. J. Solids Struct. 45 (3), 1101–1123. doi:10.1016/j.ijsolstr.2007.07.016.

Ai, J., Chen, J.-F., Rotter, J.M., Ooi, J.Y., 2011. Assessment of rolling resistance models in discrete element simulations. Powder. Technol. 206 (3), 269–282. doi:10.1016/j.powtec.2010.09.030.

Alonso-Marroquín, F., Luding, S., Herrmann, H.J., Vardoulakis, I., 2005. Role of anisotropy in the elastoplastic response of a polygonal packing. Phys. Rev. E 71, 051304. doi:10.1103/PhysRevE.71.051304.

Anandarajah, A., Sobhan, K., Kuganenthira, N., 1995. Incremental stress-strain behavior of granular soil. J. Geotech. Eng. 121 (1), 57–68. doi:10.1061/(ASCE)0733-9410(1995)121:1(57).

Andò, E., Viggiani, G., Hall, S., Desrues, J., 2013. Experimental micro-mechanics of granular media studied by x-ray tomography: recent results and challenges. Géotech. Lett. 3 (3), 142–146. doi:10.1680/geolett.13.00036.

ASTM International, Standard test methods for maximum index density and unit weight of soils using a vibratory table, West Conshohocken, PA (2006) URL www.astm.org.

ASTM International, Astm d4254-16, standard test methods for minimum index density and unit weight of soils and calculation of relative density, West Conshohocken, PA (2016) URL www.astm.org.

Bagi, K., 1996. Stress and strain in granular assemblies. Mech. Mater. 22 (3), 165–177. doi:10.1016/0167-6636(95)00044-5.

Bagi, K., 2006. Analysis of microstructural strain tensors for granular assemblies. Int. J. Solids Struct. 43 (10), 3166–3184. doi:10.1016/j.ijsolstr.2005.07.016.

Bardet, J., 1994. Numerical simulations of the incremental responses of idealized granular materials. Int. J. Plast. 10 (8), 879–908. doi:10.1016/0749-6419(94)90019-1.

Buarque de Macedo, R., Marshall, J.P., Andrade, J.E., 2018. Granular object morphological generation with genetic algorithms for discrete element simulations. Granular Matter 20 (4), 73. doi:10.1007/s10035-018-0845-7.
Calvetti, F., Viggiani, G., Tamagnini, C., 2003. A numerical investigation of the incremental behavior of granular soils. Rivista Italiana di Geotecnica 37, 11–29.
Calvetti, F., Viggiani, G., Tamagnini, C., 2003. Micromechanical inspection of constitutive modelling. In: Constitutive Modelling and Analysis of Boundary Value Problems in Geotechnical Engineering. Napoli, Italy, pp. 187–216.
Cavarretta, I., Coop, M., O'Sullivan, C., 2010. The influence of particle characteristics on the behaviour of coarse grained soils. Géotechnique 60 (6), 413–423. doi:10.1680/geot.2010.60.6.413.
CEGEO, Saint-Cyr, B., Szarf, K., Voivret, C., Azéma, E., Richefeu, V., Delenne, J.-Y., Combe, G., Nouguier-Lehon, C., Villard, P., Sornay, P., Chaze, M., Radjai, F., 2012. Particle shape dependence in 2d granular media. EPL 98 (4), 44008. doi:10.1209/0295-5075/98/44008.
Chang, C., Hicher, P.-Y., 2005. An elasto-plastic model for granular materials with microstructural consideration. Int. J. Solids Struct. 42 (14), 4258–4277. doi:10.1016/j.ijsolstr.2004.09.021.
Chang, C.S., Chang, Y., Kabir, M.G., 1992. Micromechanics modeling for stress strain behavior of granular soils. I: theory. J. Geotech. Eng. 118 (12), 1959–1974. doi:10.1061/(ASCE)0733-9410(1992)118:12(1959).
Chang, C.S., Misra, A., Acheampong, K., 1992. Elastoplastic deformation for particulates with frictional contacts. J. Eng. Mech. 118 (8). doi:10.1061/(ASCE)0733-9399(1992)118:8(1692).
Chang, C.S., Deng, Y., Yang, Z., 2017. Modeling of minimum void ratio for granular soil with effect of particle size distribution. J. Eng. Mech. 143 (9), 04017060. doi:10.1061/(ASCE)EM.1943-7889.0001270.
Christoffersen, J., Hutchinson, J., 1979. A class of phenomenological corner theories of plasticity. J. Mech. Phys. Solids 27 (5), 465–487. doi:10.1016/0022-5096(79)90026-7.
Christoffersen, J., Mehrabadi, M.M., Nemat-Nasser, S., 1981. A micromechanical description of granular material behavior. J. Appl. Mech. 48 (2), 339–344. doi:10.1115/1.3157619.
Cil, M., Alshibli, K., Kenesei, P., 2017. 3D experimental measurement of lattice strain and fracture behavior of sand particles using synchrotron x-ray diffraction and tomography. J. Geotech. Geoenviron. Eng. 143 (9), 04017048. doi:10.1061/(ASCE)GT.1943-5606.0001737.
Cole, D.M., Peters, J.F., 2007. A physically based approach to granular media mechanics: grain-scale experiments, initial results and implications to numerical modeling. Granular Matter 9 (5), 309. doi:10.1007/s10035-007-0046-2.
Collins, I.F., Einav, I., 2005. On the validity of elastic/plastic decompositions in soil mechanics. In: Proceedings of Symposium on Elastoplasticity for Prof. K. Hashiguchi Retirement Anniversary, Kyushu University, JAPAN.
Collins, I.F., Houlsby, G.T., 1997. Application of thermomechanical principles to the modelling of geotechnical materials. Proc. R. Soc. London Ser.A 453 (1964), 1975–2001. doi:10.1098/rspa.1997.0107.
Cundall, P.A., Strack, O.D.L., 1979. A discrete numerical model for granular assemblies. Géotechnique 29 (1), 47–65. doi:10.1680/geot.1979.29.1.47.
Doanh, T., Ibraim, E., 2000. Minimum undrained strength of Hostun RF sand. Géotechnique 50 (4), 377–392. doi:10.1680/geot.2000.50.4.377.
Drucker, D.C., Prager, W., 1952. Soil mechanics and plastic analysis or limit design. Q. Appl. Math. 10 (2), 157–165.
Emeriault, F., Cambou, B., Mahboubi, A., 1996. Homogenization for granular materials: non reversible behaviour. Mech. Cohesive-Frict. Mater. 1 (2), 199–218. doi:10.1002/(SICI)1099-1484(199604)1:2<199::AID-CFM10>3.0.CO;2-Y.
Froiio, F., Roux, J., 2010. Incremental response of a model granular material by stress probing with DEM simulations. AIP Conf Proc 1227 (1), 183–197. doi:10.1063/1.3435388.
Gudehus, G., 1979. A comparison of some constitutive laws for soils under radially symmetric loading and unloading. In: 3rd International Conference of Numerical Methods in Geomechanics, 4, pp. 1309–1324.
Hueckel, T., 1976. Coupling of elastic and plastic deformations of bulk solids. Meccanica 11 (4), 227–235. doi:10.1007/BF02128296.
Jenkins, J., Johnson, D., Ragione, L.L., Makse, H., 2005. Fluctuations and the effective moduli of an isotropic, random aggregate of identical, frictionless spheres. J. Mech. Phys. Solids 53, 197–225. doi:10.1016/j.jmps.2004.06.002.
Jenkins, J.T., Koenders, M., 2004. The incremental response of random aggregates of identical round particles. Eur. Phys. J. E 13 (2), 113–123. doi:10.1140/epje/e2004-00048-9.
Karapiperis, K., Marshall, J., Andrade, J., 2020. Reduced gravity effects on the strength of granular matter: dem simulations versus experiments. J. Geotech. Geoenviron. Eng. 146 (5), 06020005. doi:10.1061/(ASCE)GT.1943-5606.0002232.
Kawamoto, R., Andò, E., Viggiani, G., Andrade, J.E., 2016. Level set discrete element method for three-dimensional computations with triaxial case study. J. Mech. Phys. Solids 91, 1–13. doi:10.1016/j.jmps.2016.02.021.
Kawamoto, R., Andò, E., Viggiani, G., Andrade, J.E., 2018. All you need is shape: predicting shear banding in sand with LS-DEM. J. Mech. Phys. Solids 111, 375–392. doi:10.1016/j.jmps.2017.10.003.
Kuhn, M.R., Daouadji, A., 2018. Quasi-static incremental behavior of granular materials: elastic-plastic coupling and micro-scale dissipation. J. Mech. Phys. Solids 114, 219–237. doi:10.1016/j.jmps.2018.02.019.
Kuhn, M.R., Daouadji, A., 2018. Multi-directional behavior of granular materials and its relation to incremental elasto-plasticity. Int. J. Solids Struct. 152–153, 305–323. doi:10.1016/j.ijsolstr.2018.07.005.
Lade, P., Duncan, J., 1973. Cubical triaxial tests on cohesionless soil. J. Geotech. Geoenviron. Eng. 101, 491–493.
Lade, P.V., 1977. Elasto-plastic stress-strain theory for cohesionless soil with curved yield surfaces. Int. J. Solids Struct. 13 (11), 1019–1035. doi:10.1016/0020-7683(77)90073-7.
Li, L., Marteau, E., Andrade, J., 2019. Capturing the inter-particle force distribution in granular material using LS-DEM. Granular Matter 21 (3), 43. doi:10.1007/s10035-019-0893-7.
Liao, C.-L., Chang, T.-P., Young, D.-H., Chang, C.S., 1997. Stress-strain relationship for granular materials based on the hypothesis of best fit. Int. J. Solids Struct. 34 (31), 4087–4100. doi:10.1016/S0020-7683(97)00015-2.
Luding, S., 2005. Anisotropy in cohesive, frictional granular media. J. Phys. 17 (24), S2623–S2640. doi:10.1088/0953-8984/17/24/017.
Matsuoka, H., Nakai, T., 1974. Stress-deformation and strength characteristics of soil under three different principal stresses. Proc. Jpn. Soc. Civ.Eng. 1974 (232), 59–70. doi:10.2208/jscej1969.1974.232_59.
Misra, A., Chang, C.S., 1993. Effective elastic moduli of heterogeneous granular solids. Int. J. Solids Struct. 30 (18), 2547–2566. doi:10.1016/0020-7683(93)90165-4.
Nardelli, V., Coop, M.R., 2018. The experimental contact behaviour of natural sands: normal and tangential loading. Géotechnique 0 (0), 1–15. doi:10.1680/jgeot.17.P.167.
Nicot, F., Darve, F., RNVO Group: Natural Hazards and Vulnerability of Structures, 2005. A multi-scale approach to granular materials. Mech. Mater. 37 (9), 980–1006. doi:10.1016/j.mechmat.2004.11.002.
Oda, M., Iwashita, K., 2000. Study on couple stress and shear band development in granular media based on numerical simulation analyses. Int. J. Eng. Sci. 38 (15), 1713–1740. doi:10.1016/S0020-7225(99)00132-9.
Onsager, L., 1931. Reciprocal relations in irreversible processes. I. Phys. Rev. 37, 405–426. doi:10.1103/PhysRev.37.405.
Ortiz, M., 2012. Continuum Mechanics Lecture Notes. California Institute of Technology.
Osher, S., Fedkiw, R., 2003. Level Set Methods and Dynamic Implicit Surfaces. Springer Verlag.
O'Sullivan, C., 2011. Particulate Discrete Element Modelling: A Geomechanics Perspective. CRC Press, New York.
Plassiard, J.-P., Belheine, N., Donzé, F.-V., 2009. A spherical discrete element model: calibration procedure and incremental response. Granular Matter 11 (5), 293–306. doi:10.1007/s10035-009-0130-x.
Radjai, F., Wolf, D.E., Jean, M., Moreau, J.-J., 1998. Bimodal character of stress transmission in granular packings. Phys. Rev. Lett. 80, 61–64. doi:10.1103/PhysRevLett.80.61.

Ragione, L.L., 2016. The incremental response of a stressed, anisotropic granular material: loading and unloading. J. Mech. Phys. Solids 95, 147–168. doi:10.1016/j.jmps.2016.05.031.
Reddy, K.R., Saxena, S.K., Budiman, J.S., 1992. Development of a true triaxial testing apparatus. Geotech. Test. J. (ASTM) 15 (2), 89–105. doi:10.1520/GTJ10231J.
Richefeu, V., Combe, G., Viggiani, G., 2012. An experimental assessment of displacement fluctuations in a 2d granular material subjected to shear. Géotech. Lett. 2 (3), 113–118.
Royis, P., Doanh, T., 1998. Theoretical analysis of strain response envelopes using incrementally non-linear constitutive equations. Int. J. Numer. Anal. Methods Geomech. 22 (2), 97–132. doi:10.1002/(SICI)1096-9853(199802)22:2<97::AID-NAG911>3.0.CO;2-Z.
Sadrekarimi, A., Olson, S.M., 2010. Particle damage observed in ring shear tests on sands. Can. Geotech. J. 47 (5), 497–515. doi:10.1139/T09-117.
Salot, C., Gotteland, P., Villard, P., 2009. Influence of relative density on granular materials behavior: DEM simulations of triaxial tests. Granular Matter 11 (4), 221–236. doi:10.1007/s10035-009-0138-2.
Senetakis, K., Coop, M.R., Todisco, M.C., 2013. The inter-particle coefficient of friction at the contacts of Leighton Buzzard sand quartz minerals. Soils Found. 53 (5), 746–755. doi:10.1016/j.sandf.2013.08.012.
Tamagnini, C., Viggiani, G., 2002. On the incremental nonlinearity of soils. Part i: theoretical aspects. Rivista Italiana di Geotecnica 36 (1), 44–61.
Tamagnini, C., Calvetti, X., Viggiani, G., 2005. An assessment of plasticity theories for modeling the incrementally nonlinear behavior of granular soils. J. Eng. Math. 52, 265–291.
Thornton, C., 2000. Numerical simulations of deviatoric shear deformation of granular media. Géotechnique 50 (1), 43–53. doi:10.1680/geot.2000.50.1.43.
Tordesillas, A., Muthuswamy, M., 2008. A thermomicromechanical approach to multiscale continuum modeling of dense granular materials. Acta Geotech. 3 (3), 225–240. doi:10.1007/s11440-008-0080-1.
Vaid, Y.P., Negussey, D., 1984. Relative density of pluviated sand samples. Soils Found. 24 (2), 101–105. doi:10.3208/sandf1972.24.2_101.
Vlahinić, I., Andò, E., Viggiani, G., Andrade, J., 2014. Towards a more accurate characterization of granular media: extracting quantitative descriptors from tomographic images. Granular Matter 16 (1), 9–21. doi:10.1007/s10035-013-0460-6.
Walsh, S., Tordesillas, A., Peters, J., 2007. Development of micromechanical models for granular media. Granular Matter 9 (5), 337. doi:10.1007/s10035-007-0043-5.
Wan, R., Pinheiro, M., 2013. On the validity of the flow rule postulate for geomaterials. Int. J. Numer. Anal. Methods Geomech. 38 (8), 863–880. doi:10.1002/nag.2242.
Ziegler, H., 1977. An introduction to thermomechanics. Appl. Math. Mech. 21.